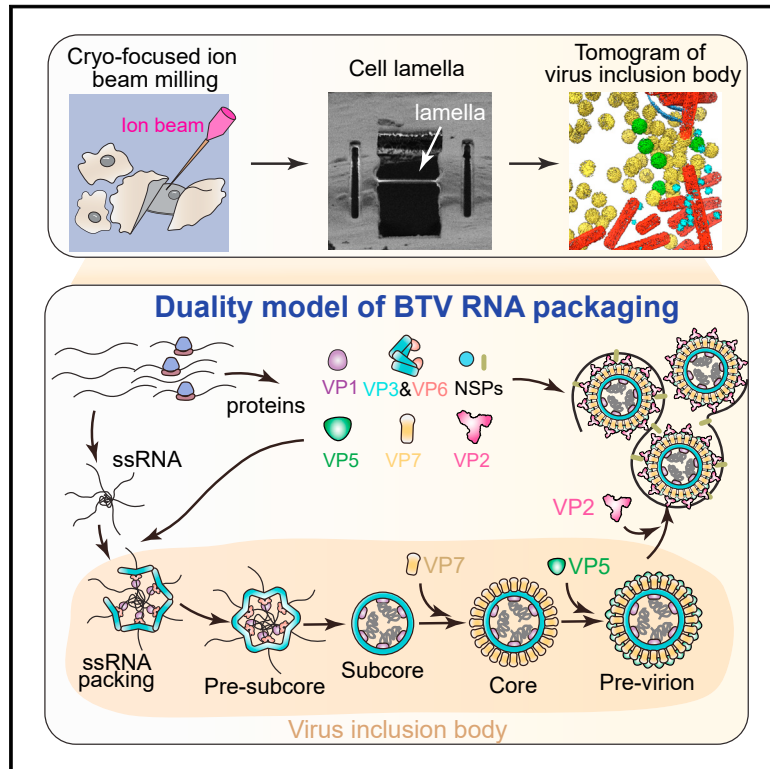


# RNA genome packaging and capsid assembly of bluetongue virus visualized in host cells

## Graphical abstract



## Authors

Xian Xia, Po-Yu Sung,  
Michael W. Martynowycz, Tamir Gonen,  
Polly Roy, Z. Hong Zhou

## Correspondence

hong.zhou@ucla.edu

## In brief

Integrated structural analyses captured a total of eleven assembly states of bluetongue virus (BTV), revealing insights into the mysterious RNA packaging and capsid assembly of dsRNA viruses.

## Highlights

- Capsid assembly of BTV in host cells visualized by cryo-FIB-based cellular cryo-ET
- High-resolution structures of BTV assembly intermediates by single-particle cryo-EM
- ATPase VP6 pentamer bound underneath the VP3 shell of the pre-subcore for RNA threading
- Duality model for BTV RNA packaging with features of both dsDNA and ssRNA viruses



## Article

# RNA genome packaging and capsid assembly of bluetongue virus visualized in host cells

Xian Xia,<sup>1,2</sup> Po-Yu Sung,<sup>3</sup> Michael W. Martynowycz,<sup>4,5</sup> Tamir Gonen,<sup>4,5</sup> Polly Roy,<sup>3</sup> and Z. Hong Zhou<sup>1,2,6,\*</sup><sup>1</sup>Department of Microbiology, Immunology and Molecular Genetics, University of California, Los Angeles, Los Angeles, CA 90095, USA<sup>2</sup>California NanoSystems Institute, University of California, Los Angeles, Los Angeles, CA 90095, USA<sup>3</sup>Department of Infection Biology, London School of Hygiene and Tropical Medicine, London WC1E 7HT, UK<sup>4</sup>Howard Hughes Medical Institute, University of California, Los Angeles, Los Angeles, CA 90095, USA<sup>5</sup>Department of Biological Chemistry, University of California, Los Angeles, Los Angeles, CA 90095, USA<sup>6</sup>Lead contact\*Correspondence: [hong.zhou@ucla.edu](mailto:hong.zhou@ucla.edu)<https://doi.org/10.1016/j.cell.2024.03.007>

## SUMMARY

Unlike those of double-stranded DNA (dsDNA), single-stranded DNA (ssDNA), and ssRNA viruses, the mechanism of genome packaging of dsRNA viruses is poorly understood. Here, we combined the techniques of high-resolution cryoelectron microscopy (cryo-EM), cellular cryoelectron tomography (cryo-ET), and structure-guided mutagenesis to investigate genome packaging and capsid assembly of bluetongue virus (BTV), a member of the *Reoviridae* family of dsRNA viruses. A total of eleven assembly states of BTV capsid were captured, with resolutions up to 2.8 Å, with most visualized in the host cytoplasm. ATPase VP6 was found underneath the vertices of capsid shell protein VP3 as an RNA-harboring pentamer, facilitating RNA packaging. RNA packaging expands the VP3 shell, which then engages middle- and outer-layer proteins to generate infectious virions. These revealed “duality” characteristics of the BTV assembly mechanism reconcile previous contradictory co-assembly and core-filling models and provide insights into the mysterious RNA packaging and capsid assembly of *Reoviridae* members and beyond.

## INTRODUCTION

Unlike the genomes of cells, which universally use double-stranded DNA (dsDNA), the genomes of viruses can be either DNA or RNA and in either ds or single-stranded (ss) forms. Genome packaging is well understood for dsDNA and ssDNA viruses, in which either dsDNA duplex or unwound ssDNA, respectively, is inserted into a pre-formed proteinaceous capsid across a vertex of the capsid through an ATP-driven process.<sup>1–3</sup> Genome packaging for ssRNA viruses does not involve ATP hydrolysis; instead, ssRNA can serve as a scaffold and co-assemble with viral proteins to form ssRNA viruses.<sup>4–7</sup> However, without *in situ* viral structures of active genome-packaging and capsid-assembling events and high-resolution structures of assembly intermediates, our understanding of genome packaging of dsRNA viruses remains incomplete, as reflected by the sharply different models proposed.<sup>8</sup> For example, the core-filling model posits that RNA is inserted into a pre-formed capsid,<sup>9</sup> a mechanism akin to that of the dsDNA viruses; on the contrary, the co-assembly model posits that viral proteins and RNA coalesce to form a capsid.<sup>10–12</sup> Understanding of the RNA packaging and capsid assembly mechanism of dsRNA virus is important not only for bridging the knowledge gap of this basic and essential process of viral replication and spread but also for designing vaccines and drugs to combat these viruses.<sup>13,14</sup>

Viruses in the family of *Reoviridae* are among the most extensively studied dsRNA viruses and infect a wide range of hosts, ranging from humans to insects and plants. Of the greatest public health concerns among these viruses are rotavirus and bluetongue virus (BTV), which cause diarrhea in humans and deaths in livestock, respectively.<sup>15</sup> Often used as model systems in studying dsRNA viruses, both BTV and rotavirus belong to the non-turreted subfamily (*Sedoreovirinae*) of *Reoviridae*. The BTV virion is composed of three layers of capsid proteins surrounding a genome of 10 dsRNA segments, which encode seven structural proteins (VP1–VP7) and four non-structural proteins (NS1–NS4).<sup>11</sup> The structures of the BTV core and virion have been determined to near-atomic resolution by X-ray crystallography and cryoelectron microscopy (cryo-EM).<sup>16–18</sup> The single-layered BTV subcore is composed of 60 VP3 dimers arranged in a T = 2 icosahedral lattice encapsulating the dsRNA genome, referred to as the subcore. The subcore is stabilized by an assembly of 260 VP7 trimers in a T = 13 icosahedral lattice in the middle layer, resulting in the double-layered core.<sup>11</sup> The BTV virion contains three layers of capsid proteins, with 120 globular trimers of VP5 and 60 triskelion-like VP2 trimers interdigitating one another in the outer layer.<sup>17</sup> Cryo-EM results from icosahedral-structure-guided sub-particle reconstructions showed that, in the core and virion, one copy of polymerase VP1 binds to the VP3 shell at each vertex inside the capsid near the icosahedral 5-fold axis.<sup>16</sup>



Biochemical experiments have demonstrated that the minor protein VP6 is an ATPase and RNA helicase<sup>19</sup> and is essential for the packaging of 10 ssRNA segments into the capsid,<sup>20,21</sup> where the ssRNA segments are replicated into dsRNA by polymerase VP1. Despite this structural knowledge of these three forms of BTV capsids, the physiological significance and the temporal order of the various capsid forms have not been established. Additionally, how newly synthesized ssRNA segments are packaged within the capsid subcore is still disputed due to the difficulty of studying these intra-cellular and dynamic events, which has resulted in a complete absence of high-resolution structures of assembly intermediates for these viruses.

Here, we used a combination of cellular cryo-ET, high-resolution single-particle cryo-EM, and structure-guided mutagenesis to investigate BTV replication and capsid assembly within cultured cells. By capturing a total of eleven assembly states of BTV by cryo-EM and cryo-ET, we revealed the structural basis of VP6-facilitated ssRNA packaging and suggested a duality model of BTV capsid assembly that has features of genome packaging mechanisms of both dsDNA and ssRNA viruses. These results provide general insight into the mysterious assembly of *Reoviridae* members and beyond and may contribute to the development of antiviral drugs against these viruses.

## RESULTS

### Cellular cryo-ET captures BTV assembly intermediates with and without RNA

To investigate the sequential processes of BTV assembly in host cells, we grew baby hamster kidney (BHK21) cells on gold EM grids and infected them with BTV (see [STAR Methods](#)). The cells were plunge-frozen in liquid ethane, and thin lamellae with thicknesses of around 250 nm were generated by cryogenic focused ion beam (cryo-FIB) milling ([Figures 1A and 1B](#)). Cryo-ET reconstructions (tomograms) from these lamellae show tubes formed by BTV non-structural protein NS1,<sup>22</sup> clear features of different virus capsids, and ribosomes and vesicles from the host cells ([Figures 1C–1H and S1](#)).

During the BTV replication cycle, non-structural protein NS1 regulates protein synthesis, while non-structural protein NS2 engages the viral genome and structural proteins in the virus inclusion body (VIB), where virus assembly occurs.<sup>23</sup> The tomograms ([Figures 1E and 1F](#)) show that the VIB is a non-membrane-bounded condensate of viral capsids. These viral capsids were observed to have different layers of proteins and different RNA densities inside and were identified as assembly intermediates of the BTV virion ([Figure 1I](#)). Similar viral capsid structures were also observed in BTV-infected cells in the early stage ([Figure S1I](#)).

The BTV virion comprises three layers of viral proteins. First, a single-layered capsid with a diameter of around 55 nm was observed inside the cell, composed of a thin protein shell with weak density inside ([Figures 1C, 1D, and 1I](#)). This single-layered capsid represents the innermost protein layer and is designated as the pre-subcore, as compared with the subcore. A second, double-layered capsid, with a spiky surface and a diameter of ~68 nm, was identified inside the VIB as the BTV core ([Figure 1E, 1F, and 1I](#); [Video S1](#)). The core is formed by VP7, layered over the

pre-subcore. A third, triple-layered ~72-nm-diameter capsid had a smooth surface; it represents the pre-irion state, with outer-layer protein VP5 assembled on top of middle-layer VP7, also in the VIB ([Figures 1E, 1F, and 1I](#); [Video S1](#)). This observation of the pre-irion in VIB is consistent with previous results from light microscopy, which showed that outer-layer protein VP5 is associated with VIBs, facilitating virus maturation.<sup>24</sup> Outside the VIB, VP2 attaches to the capsid's outer layer of VP5, forming the complete irion ([Figures 1G–1I and S1A](#)). The transmembrane protein NS3 was suggested to bridge the immature capsids and VP2 and to bring the newly formed irion to the plasma membrane,<sup>25,26</sup> facilitating the virus egress process. In line with this, we observed virion particles interacting with the membrane ([Figures 1G, 1H, S1B, and S1C](#); [Video S2](#)). This interaction is confirmed by subtomogram averaging, which shows VP2 tip domain in the vicinity of the membrane ([Figure S1D](#)). The membrane that interacts with BTV virions near the edge of the host cell is fragmented, indicating that the outermost capsid protein VP2 can destabilize the cell membrane and may facilitate virus egress. In total, by cellular tomography, we captured six states of BTV assembly in host cells ([Figures 1I and S1E–S1H](#); [Table S1](#)) with resolutions up to 7.2 Å, which allows us to correlate these assembly states with high-resolution cryo-EM structures (described below) to infer the process of virus assembly and egress.

### High-resolution structures of assembly intermediates of BTV

Next, to identify and resolve interactions between protein and RNA within these assembly states for functional interpretation, we performed single-particle cryo-EM on viral isolates that were enriched from infected cells by a simple sucrose cushion step. Cryo-EM images and images from 2D classification show clear features of different assembly states, including single-layered, double-layered, and triple-layered particles ([Figures S2A and S2B](#)). These particles were further analyzed by 3D classification, resulting in a total of eight different assembly states: single-layered pre-subcore and subcore; double-layered pre-core (VP7 missing around the 5-fold axis) and core; triple-layered irion; and three empty capsids (empty pre-core, empty core, and empty irion), the byproducts of failed genomic RNA packaging ([Figures 2A and S2C](#)). Compared with the intermediates identified from cellular cryo-ET, the pre-irion, containing the outer-layer VP5, was not found in the isolates by the current workflow, whereas the dsRNA-filled, single-layered capsid, the subcore, was sorted out from the isolates. The number of subcore particles (177) is less than 1% of that of both the pre-subcore and pre-core in the isolates, indicating the transient existence of this state. The number of empty capsids is less than 20% of all picked particles, suggesting that binding of genomic RNA facilitates virus assembly.

To improve the resolution of these capsid assembly intermediates, we performed icosahedral-structure-guided sub-particle reconstruction ([Figure S2C](#)). For the pre-subcore, two conformations that differed in invagination at the 5-fold axis were sorted out by classification. The conformation (Conf1), which has a higher resolution and better map densities, is used for further analysis in this paper ([Figures S2C and S2F](#)). The local resolution



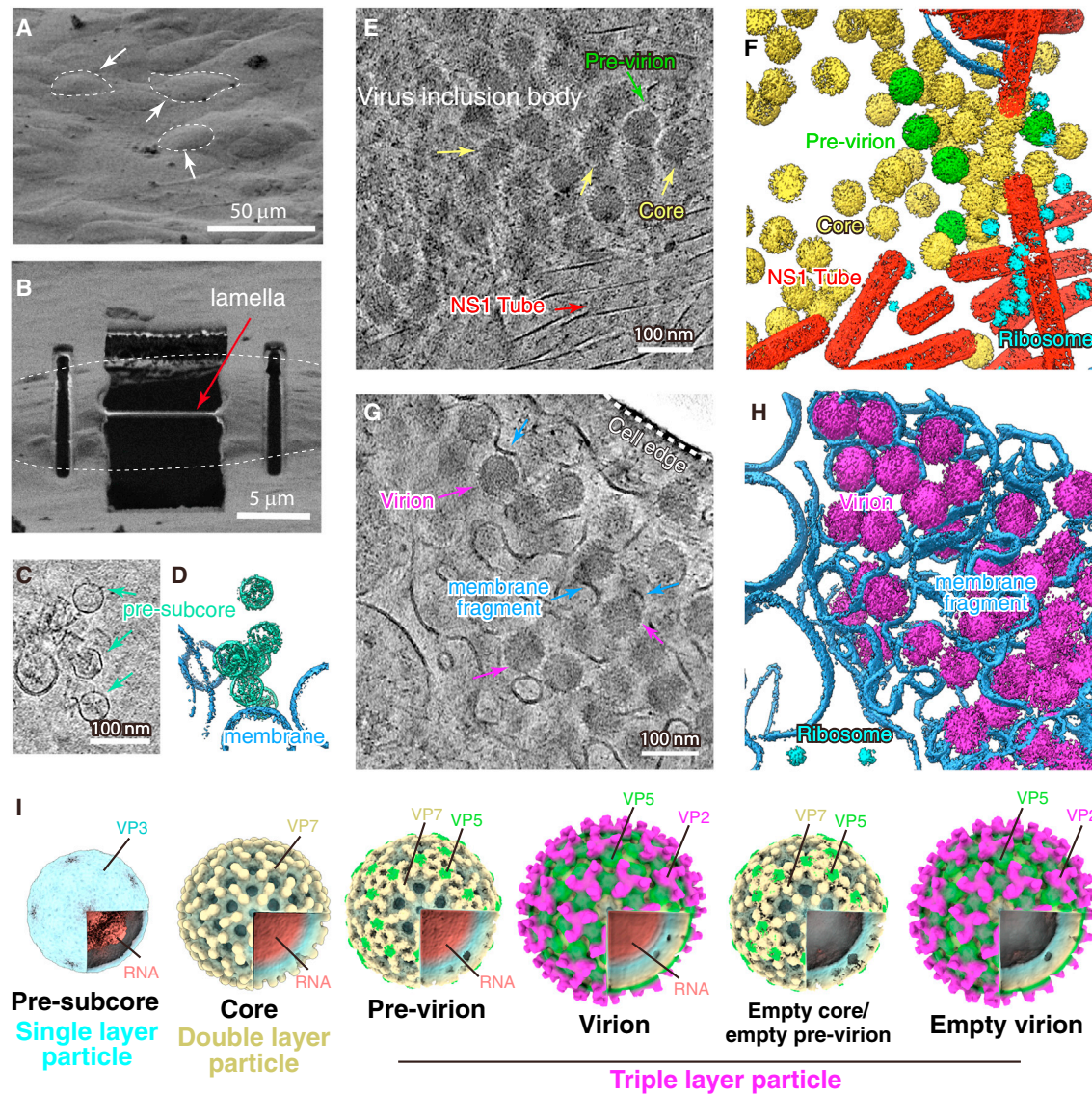


**Figure 1. BTV assembly intermediates in the host cytoplasm captured by cellular cryo-ET**

(A) Scanning electron microscope (SEM) image of infected cells on EM grid prior to cryo-FIB milling. Example cells are outlined by dashed lines and indicated by arrows.

(B) SEM image of a cell after FIB milling. Outline of the cell is indicated by dashed lines.

(C and D) A slice image (C) and corresponding 3D segmentation (D) from the cryo-ET reconstruction, showing the assembled pre-subcore.

(E and F) A slice image (E) and corresponding 3D segmentation (F) from a cryo-ET reconstruction, showing the BTV assembly intermediates within a virus inclusion body.

(G and H) A slice image (G) and corresponding 3D segmentation (H) of cryo-ET reconstruction, showing that virus egress is associated with membranes at the cell periphery.

(I) Six states of BTV assembly captured by cellular tomography.

See also [Figure S1](#) and [Video S1](#) related to (E) and (F) and [Video S2](#) related to (G) and (H).

map of the pre-subcore also shows flexibility at the 5-fold axis ([Figure S2G](#)), indicating that the structure of the pre-subcore may be able to adopt different invagination levels during RNA packaging. For the pre-core, core, and virion, structures of VP1 were resolved by local classification, with a mask at 5-fold axis utilizing previously reported methods ([Figure 2B](#)).<sup>16</sup> Similar densities of VP1 at the 5-fold axis in the subcore are visible,

though not well resolved ([Figure 2B](#)). In the empty particles (empty pre-core, empty core, and empty virion), no extra densities at the 5-fold axis were observed, even after local classification ([Figure S2C](#)), suggesting that VP1 is absent from these assembly states. Final sub-particle reconstructions of the eight assembly states were obtained at resolutions ranging from 2.8 to 6.5 Å ([Figures S2C–S2H](#); [Table S2](#)). The structural features





of the capsid protein VP7 and outer-layer proteins VP5 and VP2 match the previously solved cryo-EM structures of the BTV core and virion,<sup>16,17</sup> with the addition of full-length model building of VP2, including the previously unmodeled tip domain, enabled by the higher resolution of VP2 in our cryo-EM structure. By contrast, the inner-layer protein VP3 has a drastically different conformation in the pre-subcore than in other states (detailed below). In addition, VP6, which was shown to be an ATPase and RNA helicase,<sup>19</sup> binds to the VP3 at the 5-fold axis only in the pre-subcore; the same position is occupied by VP1 in other states.

### VP6 pentamer binds underneath VP3 to create an RNA-threading tunnel in the pre-subcore

The single-layered capsid with VP3 invaginated at the 5-fold axis, identified in the cellular tomogram and resolved at atomic resolution by single-particle cryo-EM, is designated as the pre-subcore (Figures 1I and 2A). At a lower map threshold, RNA density is visible inside the capsid and in the 5-fold tunnel formed by VP3 and VP6 (Figure 3A). Unlike previous reports showing that recombinantly expressed VP6 has different oligomerization states, including hexamer,<sup>27</sup> our cryo-EM structure of native BTV particles shows that VP6 binds underneath the VP3 at the 5-fold axis as a pentamer in the pre-subcore, with each VP6 monomer binding to a VP3 dimer (Figures 3B and 3C). VP6 has two globular  $\alpha$  helix-rich domains: the capsid binding domain (CBD), formed from both N- and C-terminal regions of the VP6 sequence; and the RNA-binding domain (RBD), formed from the middle sections (Figures 3D and 3E). VP6 interacts with VP3B apical domain (the VP3 protomer away from the 5-fold axis) through its CBD, in line with previous results showing that mutations in the CBD disrupt VP3-VP6 interaction.<sup>21</sup> Although the RBD of VP6 has little contact with the capsid shell protein VP3, five VP6 RBDs form a pentameric ring surrounding the RNA density in the 5-fold tunnel (also referred to as the RNA-binding tunnel) (Figures 3F–3H). The surface of the tunnel at the 5-fold axis formed by VP3 and VP6 is about 18 Å in diameter and rich in positively charged residues, complementary to the negative charge of the bound RNA in the tunnel (Figures 3G and 3H). Six positively charged residues (R167, K171, R177, R188, R191, and K195) from each VP6 monomer and one from a VP3 (R431) monomer, totaling 35 in the pentameric ring, line the RNA-binding tunnel, providing strong interactions between the capsid proteins and the genomic RNA. To quantify the interactions between the capsid proteins and the RNA, we performed an electrophoretic mobility shift assay (EMSA; see STAR Methods) with the recombinantly co-expressed VP3 and VP6 complex and a synthetic 16-nt ssRNA (Figures 3I, S3A, and S4A). The result shows that the VP3-VP6 complex with a wild-type (WT) interface had strong RNA-binding activity, with an apparent binding affinity  $K_{1/2}$  of 192 nM. This binding activity

attenuated more than 2 times with a VP3 R431F mutation ( $K_{1/2} = 465$  nM) and 4 times with double mutations on VP6 (R167E/K171E,  $K_{1/2} = 761$  nM or R191E/K195E,  $K_{1/2} = 793$  nM). These observed VP6-RNA interactions are consistent with previous results showing that both mutation and deletion of VP6 disrupted BTV replication, leading to empty capsid formation.<sup>20</sup> Overall, these results show that the ATPase VP6 forms a pentamer underneath VP3 and binds to RNA during capsid assembly and that this binding is essential for RNA genome packaging.

### RNA binding to the VP3-VP6 tunnel promotes capsid assembly

We reason that the above-described RNA binding at the 5-fold tunnel should strengthen the protein interactions within the VP6 pentamer, thus increasing the stability of the capsid and facilitating capsid protein assembly. To test this hypothesis, we co-expressed His-tagged VP3 together with VP6 in insect cells and carried out biochemical and structural analyses of molecular complexes VP3 and VP6 form. Sodium dodecyl sulfate polyacrylamide-gel electrophoresis (SDS-PAGE) of the His-tag purified protein materials shows that VP3 and VP6 interact with each other and copurify (Figure S3A). Gel-filtration chromatography and analytical ultracentrifugation analyses indicate that VP3 and VP6 form a complex with a total molecular mass of about 460 kDa (Figures S3A–S3C), suggesting there are likely four copies of VP3 in the complex.

Next, we determined the exact molecular composition and detailed interactions between VP3 and VP6 in the above isolated complex by EM analysis. In both the original micrographs and 2D class averages, there is a predominant complex (Figures S3D and S3E) that, upon 3D reconstruction, is a VP3-VP6 heterohexamer containing a tetramer of VP3 and two copies of VP6 (Figures 4A and S3F–S3H; Table S3). The VP3-VP6 heterohexamer has C2 symmetry, with the 2-fold axis located at the interface between two VP3 dimers (VP3A<sub>1</sub>-VP3B<sub>1</sub> and VP3A<sub>2</sub>-VP3B<sub>2</sub>, left panel in Figure 4A). The dimer structure in the VP3-VP6 heterohexamer is similar to the VP3A-VP3B dimer observed in the pre-subcore (Figure 3C). Around the 2-fold axis, the dimerization domains of VP3A<sub>1</sub> and VP3B<sub>2</sub> interact, as do those of VP3B<sub>1</sub> and VP3A<sub>2</sub> (Figure 4A). Similar to the situation in the pre-subcore, VP6 binds through its CBD to the apical domain of VP3B<sub>1</sub> or VP3B<sub>2</sub>, and the two VP6 molecules in the VP3-VP6 heterohexamer have no contact with each other. The VP6 RBD is not visible in the VP3-VP6 heterohexamer, indicating its flexibility. In addition to the VP3-VP6 heterohexamer, we also observed pre-subcore-like VP3-VP6 capsid (Figures S3F and S3I). The VP3 and VP6 structures in this particle are similar to those in the pre-subcore (Figure 3B), except that no RNA density is observed and the RNA-binding domain of VP6 is not visible (Figure S3I). The electrostatic repulsion between the positively charged residues in the central

### Figure 2. High-resolution structures of BTV assembly intermediates resolved by cryo-EM

(A) Cryo-EM maps from icosahedral reconstruction of BTV assembly intermediates. Among the eight states shown in Figure S2, only five contain RNA and are shown here. For each viral particle, structures around one of the 12 vertices are colored. The red circle demarcates the area for sub-particle reconstruction. (B) Corresponding vertex reconstructions by sub-particle boxed out from the BTV assembly intermediates in (A). Densities segmented out for different protein and RNA molecules are colored differently, as labeled. See also workflow and additional assembly states in Figure S2.



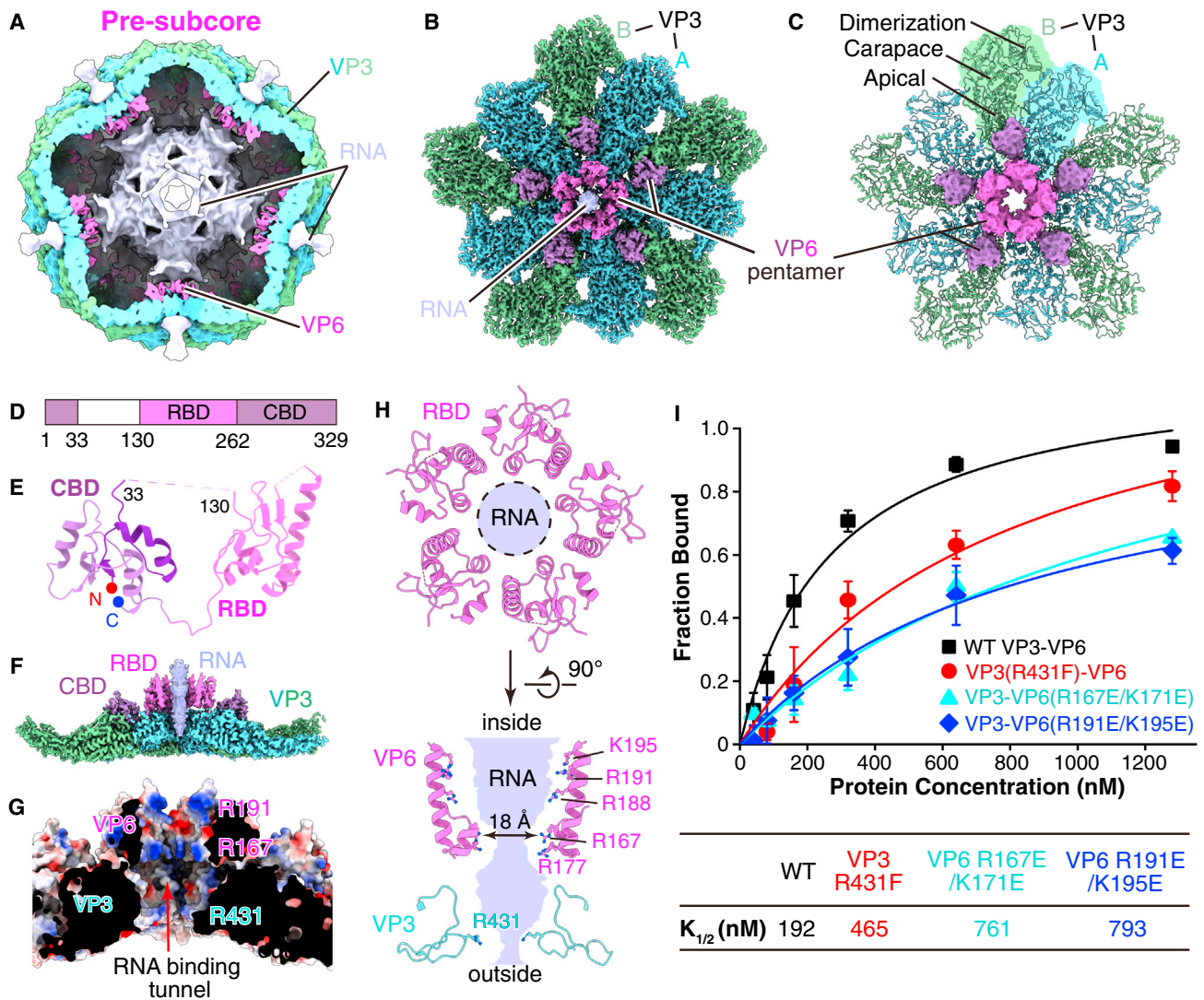


**Figure 3. VP6 pentamer binds underneath VP3 decamer to create an RNA-threading tunnel in the pre-subcore**

(A) Cut-open view of the reconstruction of the pre-subcore, showing VP6 (pink) pentamer threading the RNA (light purple) from outside to inside. (B) Cryo-EM density of VP3, VP6, and RNA in the sub-particle reconstruction from pre-subcore. The RNA density at the 5-fold axis is low-pass filtered to 20 Å and shown in light purple. (C) Atomic model of the VP6 pentamer (surface view) and the VP3 decamer (ribbons) in the pre-subcore, viewed along the same orientation as in (B). The two VP3 molecules (VP3A, cyan, and VP3B, green) are highlighted. (D and E) Domain organization (D) and atomic model (E) of VP6. RBD, RNA-binding domain; CBD, capsid binding domain. (F and G) Binding of RNA in the 5-fold tunnel formed by a VP6 pentamer and a VP3 decamer. The structure in (B) is rotated 90° and cut open to show the cryo-EM densities (F) and surface charge properties (G) of the RNA-binding tunnel. (H) RNA-protein interactions in the RNA-binding tunnel of pre-subcore. (I) RNA-binding affinity (measured by EMSA) of the recombinant complexes containing either WT or various mutations of VP3 and VP6. The apparent binding affinity  $K_{1/2}$  values were estimated from protein concentration at 50% saturation. Error bars, SD ( $n = 3$  independent measurements). See also Figures S3 and S4.

tunnel may interfere with pentamer formation in the absence of RNA. The flexibility of VP6 RBD in the absence of RNA is consistent with the small buried surface area (307 Å<sup>2</sup>) between two RBDs upon RNA binding, showing no strong interactions between the RBDs in the absence of RNA. These observations indicate that the VP3-VP6 heterohexamers are a precursor of BTV capsid assembly, and RNA is important for capsid assembly.

We then asked how RNA participates in capsid assembly. When incubated in the absence of RNA, the VP3-VP6 complex assembles into capsids, albeit with low efficiency and lack of RNA density at the 5-fold axis (Figures 4B and 4C). By contrast, incubation of VP3-VP6 in the presence of ssRNA greatly enhanced the efficiency of assembling the VP3-VP6 complex into icosahedral capsids (Figures 4B, lanes 1 and 2, 4C, S4B,



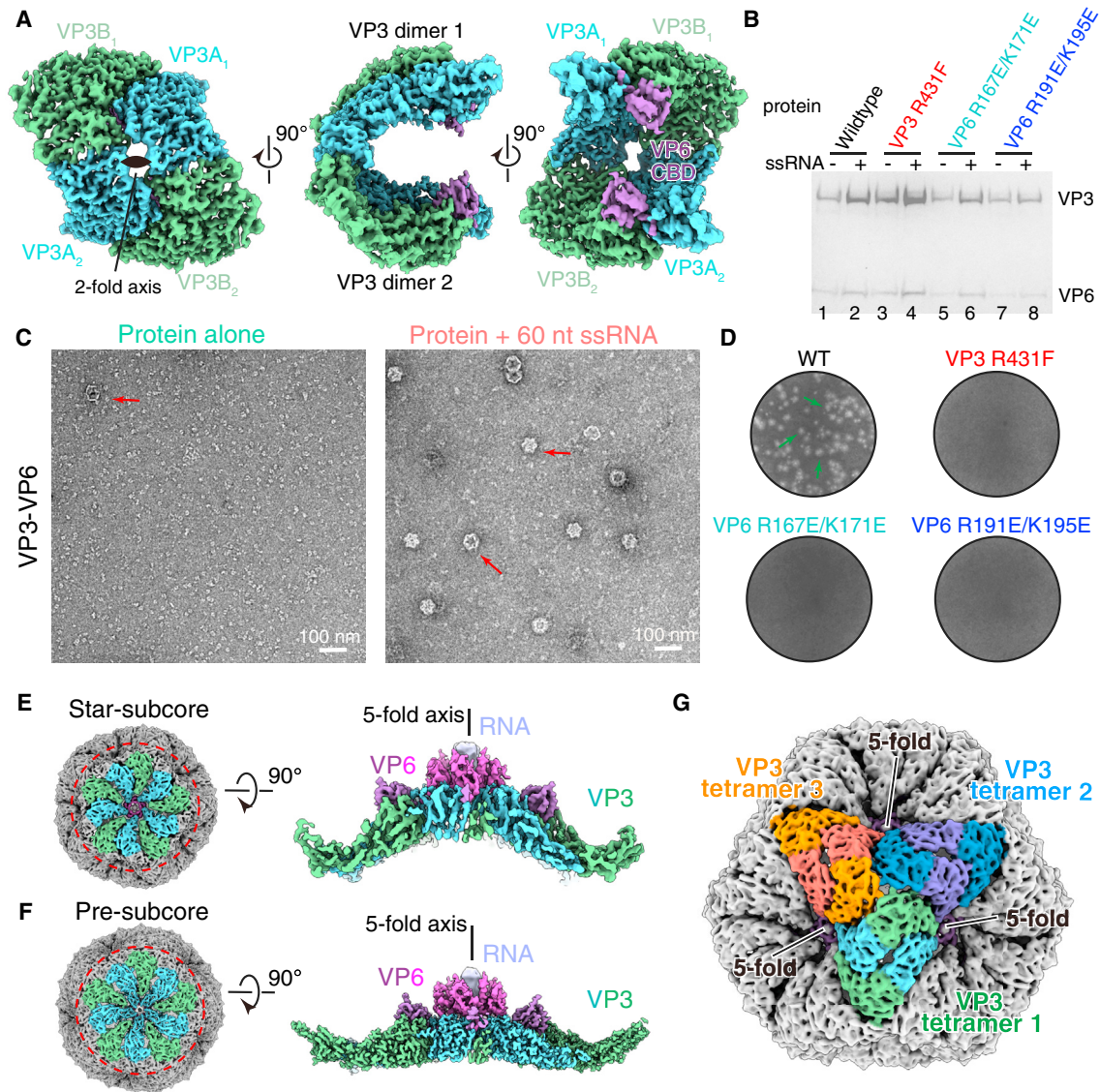


**Figure 4. RNA binding promotes the assembly of BTV**

(A) Cryo-EM structure of the recombinant VP3-VP6 complex shown as shaded surfaces colored by protein subunits.  
 (B) Coomassie blue-stained SDS-PAGE profiles of VP3-VP6 capsids *in vitro* assembled by wild-type or various mutants of VP3 and VP6 in the absence and presence of 60 nt ssRNA. Assembled capsids were pelleted by centrifugation and resolved by SDS-PAGE. Results represent three independent biological replications. Quantification was performed and shown in [Figure S4B](#).  
 (C) Negative staining TEM images of recombinant VP3-VP6 complex in the absence and presence of 60 nt ssRNA. Red arrows point to assembled capsids.  
 (D) Plaque formation at 72 h post-transfection of reverse genetics (see details in [STAR Methods](#)). RNA genome segments used were either WT or with indicated mutations on VP3 or VP6. Several plaques are indicated with green arrows.  
 (E and F) Cryo-EM reconstructions of the *in vitro*-assembled capsid using recombinant VP3-VP6 complex and 40 nt poly-U ssRNA, capturing star-subcore (E) and pre-subcore (F) conformations. Regions used for sub-particle reconstructions are indicated by the red circle.  
 (G) Structure of the star-subcore. Three VP3 tetramers are colored, together with bound RNA at 5-fold, showing the assembly of the BTV capsid.  
 See also [Figures S3, S4, and S5](#) and [Video S3](#).

and S4D). Capsid assembly was also enhanced when incubation was done in the presence of the purified BTV genome segment S10 ([Figure S4E](#)). Similar to how capsid assembly is enhanced by RNA-protein interactions, we predicted that increasing protein-protein interactions in the 5-fold tunnel should also enhance capsid assembly in the absence of RNA. Indeed, by increasing

VP3-VP3 interactions through Arg431 to Phe mutation within the tunnel ([Figure 3H](#), lower panel), we demonstrated increased capsid assembly activity—even without adding RNA ([Figure 4B](#), lanes 3 and 4). However, our structure predicts that this mutation blocks the RNA-binding tunnel; indeed, BTV bearing this mutation (VP3 R431F) failed to recover when tested with the reverse

genetics method, despite multiple attempts (Figure 4D). By contrast, proteins with a double mutation in the VP6 RNA-binding site (R167E/K171E or R191E/K195E) decrease VP6-RNA binding; as expected, VP6 carrying these mutations showed low assembly activity (30% that of WT) when incubated with RNA (Figures 4B, lanes 5–8 and S4B–S4D), and no virus was recovered when the BTV genomes carrying these two mutations were used for reverse genetics (Figure 4D). Taken together, these results from our structure-based functional studies show that RNA binding at the 5-fold tunnel is important for capsid assembly and virus replication.

Cryo-EM reconstruction of the above capsid assembled in the presence of synthetic ssRNA revealed two different icosahedral configurations of the single-layered capsid: pre-subcore (80%) and star-subcore (20%) (Figures 4E, 4F, and S5A–S5D). The structure of the pre-subcore from the *in vitro*-assembled capsid sample is the same as that of the pre-subcore from capsids isolated from infected cells, with a VP6 pentamer bound underneath the VP3 decamer at each vertex. RNA density is observed within the 5-fold tunnel but not inside the capsid (Figure 4F). As in the pre-subcore, VP6 in the star-subcore also forms a pentamer underneath VP3 and binds to RNA at the 5-fold axis (Figure 4E). However, VP3 at the 5-fold axis invaginates 55 Å further in the star-subcore than in the pre-subcore (Figures S5E and S5F). This large invagination of the capsid shell protein in the star-subcore is reminiscent of that of single-layered particles of reovirus observed *in situ* (Figure S5G).<sup>28</sup> The structures of the VP3 protomer in both the pre- and star-subcore are the same, but both VP3A and VP3B rotate outward as rigid bodies, about 30° from the star-subcore to the pre-subcore (Figure S5F; Video S3), increasing by 1.7 times the inner space encapsulated by VP3, from  $2.7 \times 10^7$  to  $4.6 \times 10^7$  Å<sup>3</sup>. Recombinant VP3-VP6 heterohexamer has the same conformation as that in the star-subcore (Figures 4A, 4G, and S5E), suggesting that the VP3-VP6 heterohexamer is an early assembly intermediate before RNA binding. Instead of VP3 being assembled into a decamer first at one vertex, the adjacent vertices are assembled simultaneously by using VP3-VP6 heterohexamers as building blocks (Figure 4G). In total, capturing the VP3-VP6 heterohexamer, star-subcore, and pre-subcore, which represent early stages in BTV capsid assembly, further supports the idea that RNA binding enhances BTV capsid assembly and that rearrangement of VP3 can lead to BTV capsid expansion during RNA packaging.

### Conformational change of VP3 results in capsid expansion during RNA packaging

In the BTV particles present in the viral isolates from infected cells, the subcore, the RNA-filled single-layered particle, was sorted out and reconstructed to 6.5 Å. The space inside the capsid is fully occupied by RNA, and more than two layers of the RNA are visible (Figures 5A and 5B). The RNA density in the subcore is comparable to that resolved in the core and virion, suggesting that genome replication from ss- to dsRNA has already occurred at this state. The VP3 of the subcore arranges in a spherical shape, without invagination at the 5-fold axis (Figures 5B and 5C), as opposed to the deep invagination in the pre-subcore mentioned above. Underneath the VP3 at each vertex, VP6 is replaced by VP1. However, due to limited

particle numbers, we were unable to resolve the asymmetry of VP1 at this state, even though VP1's smeared density is clearly visible (Figure 5B). Comparing the structures of the pre-subcore and subcore shows the conformational changes of VP3 at the 5-fold axis, expanding the inner space encapsulated by VP3 from  $4.6 \times 10^7$  Å<sup>3</sup> in the pre-subcore to  $5.5 \times 10^7$  Å<sup>3</sup> in the subcore (Figures 5D–5F; Video S4). The two VP3 subunits (VP3A and VP3B) in a dimer move differently: VP3A in the dimer rotates 40° outward, involving a hinge-like flex of 27° within the molecule, while VP3B in the dimer rotates 25° outward, involving a hinge-like flex of 16° within the molecule (Figure 5G). In addition, local structures within the VP3A and VP3B protomers also change after capsid expansion. The N-terminal  $\alpha$  helix (24–61) in VP3A is released from the VP3 apical domain to bind VP1 in the subcore (Figures S6A and S6B). Although the N-terminal  $\beta$ -hairpin (amino acids [aa] 12–24) and apical loop (aa 306–334) of VP3B dock on the surface of VP6 in the pre-subcore, they are both restructured to adapt for VP1 binding in the subcore (Figures S6C and S6D). After the capsid expansion from pre-subcore to subcore, the structure of VP3 changed to adapt VP1 binding and is no longer suitable for the binding of VP6, which will detach from the VP3 shell and remain inside the capsid. Interestingly, within the three empty states of the BTV capsid (empty pre-core, empty core, and empty virion), no density of VP1 is observed, even after local classification at the 5-fold axis, indicating that packaging of genomic RNA inside the capsid is necessary for polymerase VP1 to dock near the 5-fold axis of the inner capsid shell to interact with the N-terminal  $\alpha$  helix of VP3A. In conclusion, packaging and replication of genomic RNA segments induce the expansion of capsid shell protein VP3, accompanied by the replacement of VP6 by polymerase VP1 at the 5-fold axis.

### Stepwise assembly of middle-layer protein VP7 and outer-layer proteins VP5 and VP2

After assembly of the inner-layer protein VP3, middle-layer protein VP7 and outer-layer proteins VP5 and VP2 start to assemble on the T = 2 VP3 shell. Each BTV particle contains a total of 260 VP7 trimers in the middle layer, arranged into a T = 13 shell, with 13 trimers in each facet of the virus. The symmetry mismatch between the inner- and middle-layer proteins creates different binding sites for the 13 VP7 trimers, of which the trimer at the icosahedral 3-fold axis has the strongest interaction with VP3.<sup>29</sup> In line with this interaction, the VP7 trimer at the 3-fold axis was observed to be the first trimer assembled on the VP3 shell in the pre-subcore (Figure 6A). In the pre-core, nine VP7 trimers are subsequently assembled around that first VP7 trimer. In the core state, assembly of the VP7 layer is finished by incorporating trimers around the 5-fold axis that make the least favorable contacts with VP3. This sequential VP7 assembly is also supported by BTV capsids produced in a recombinant expression system.<sup>30,31</sup> Following the assembly of middle-layer VP7, 120 copies of VP5 trimers are stepwise incorporated into the capsid by docking into the cavities formed by six adjacent VP7 trimers, resulting in the pre-virion state. Finally, 60 copies of VP2 trimers are incorporated on top of the pre-virion, forming the virion (Figure 6B). Our cellular tomography shows that the association of VP5 in the pre-virion occurs in the VIB (Figures 1E, 1F, and 1I), while VP2 is assembled outside of the VIB. This sequential

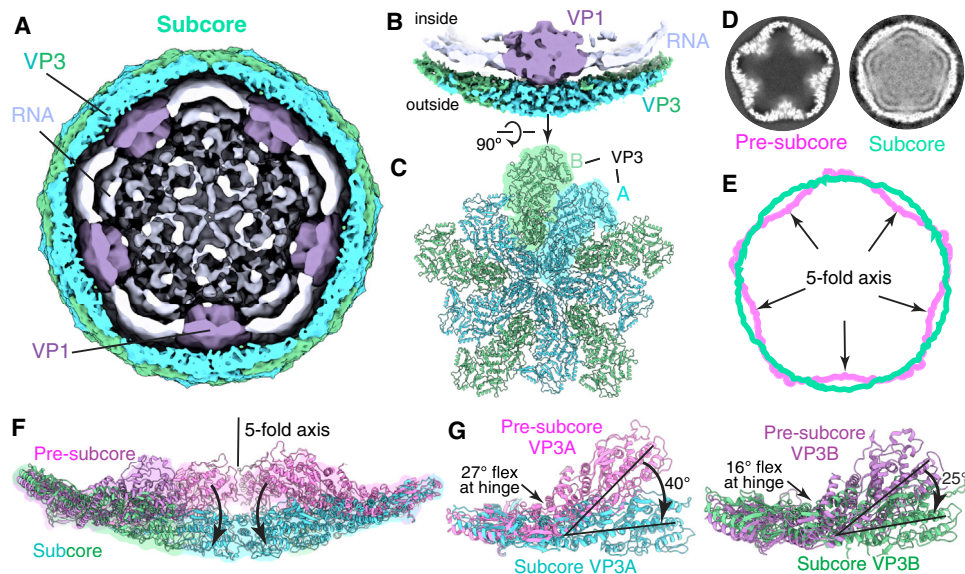


**Figure 5. Conformational changes of capsid shell protein VP3 during RNA packaging**

- (A) Cut-open view of the reconstruction of the subcore, showing the densities of RNA and polymerase VP1.  
 (B) Cryo-EM density at 5-fold vertex obtained by sub-particle reconstruction. The densities of RNA and VP1 are low-pass filtered to 20 Å.  
 (C) Atomic model of the VP3 decamer shown as ribbon. One VP3 dimer with two VP3 protomers (VP3A and VP3B) are highlighted.  
 (D) Central slices of icosahedral reconstructions of pre-subcore and subcore.  
 (E) Comparison of the shapes of pre-subcore and subcore from (D) are superposed and represented by magenta and green circle, respectively. Arrows show capsid expansion and conformational changes at 5-fold vertices.  
 (F) Structure superposition of pre-subcore and subcore showing the conformational changes of VP3 during RNA packaging. Arrows indicate the movements of VP3 at 5-fold axis.  
 (G) Conformational changes of VP3A (left) and VP3B (right) from (F).  
 See also [Figure S6](#) and [Video S4](#).

assembly of outer-layer proteins is supported by previous results of light microscopy showing that VP5, but not VP2, is associated with VBs during assembly.<sup>24,32</sup> The fully assembled BTV virions are then trafficked to interact with the host cell membrane ([Figures 1G, 1H, and S1B–S1D](#)). This interaction of VP2 with cell membrane, possibly via interactions between VP2 tip domain and NS3 (the only membrane protein of BTV),<sup>26,33,34</sup> is important for the virus egress process. The tip domain of VP2, mainly comprising  $\alpha$  helices ([Figures 6C and 6D](#)), is also important for receptor binding<sup>35</sup> during viral infection in a new virus replication cycle.

## DISCUSSION

### RNA-binding tunnel in the pre-subcore

By integrating cellular cryo-ET, single-particle cryo-EM, structure-guided mutagenesis, and *in vitro* assembly assays, we obtained and characterized a total of eleven different assembly states of the BTV capsid. These include the VP3-VP6 heterohexamers and star-subcore from *in vitro*-assembled capsids, eight different states (pre-subcore, subcore, pre-core, core, virion, empty pre-core, empty core, and empty virion) from the BTV isolate of infected cells, and pre-virion from host cytoplasm by cellular tomography. Within the eleven assembly states, the previously uncharacterized pre-subcore captured in this study is key to understanding the early stage of BTV assembly and

genomic RNA packaging. In the pre-subcore, VP6 binds underneath the VP3 shell as a pentamer and forms an RNA-binding tunnel together with VP3. RNA density is observed inside the tunnel, threading from outside to inside the BTV capsid. Mutation of VP3 Arg431 to phenylalanine blocks the RNA-binding tunnel in the pre-subcore but not the transcript exit channel in the core. Although the VP3-VP6 complex with the VP3 R431F mutation has high capsid assembly activity ([Figures 4B and S4B–S4D](#)), transfection of the BTV genome bearing this mutation failed to recover any infectious viral particles ([Figure 4D](#)). This result indicates that blocking of the RNA-binding tunnel in the pre-subcore may stop RNA threading and packaging and further supports the essential role of the RNA-binding tunnel to BTV replication. VP6 is an ATPase and RNA helicase<sup>19</sup> that binds to RNA in the 5-fold tunnel, suggesting that VP6 functions as a motor to thread the ssRNA segments into the pre-subcore. However, RNA polymerase VP1 may also have functions in this process as it is essential for capsid assembly,<sup>36</sup> despite being unresolved in the pre-subcore structure ([Figure 3A](#)).

Our results point to both shared and divergent features across viruses in the large family of *Reoviridae*. The star-subcore and pre-subcore of BTV, an unturreted member of the *Reoviridae*, resemble the star-shaped, single-layered particles of turreted reovirus<sup>28</sup> and unturreted rotavirus<sup>37</sup> observed in cellular tomography. This suggests that the RNA packaging and capsid assembly processes in both unturreted and turreted



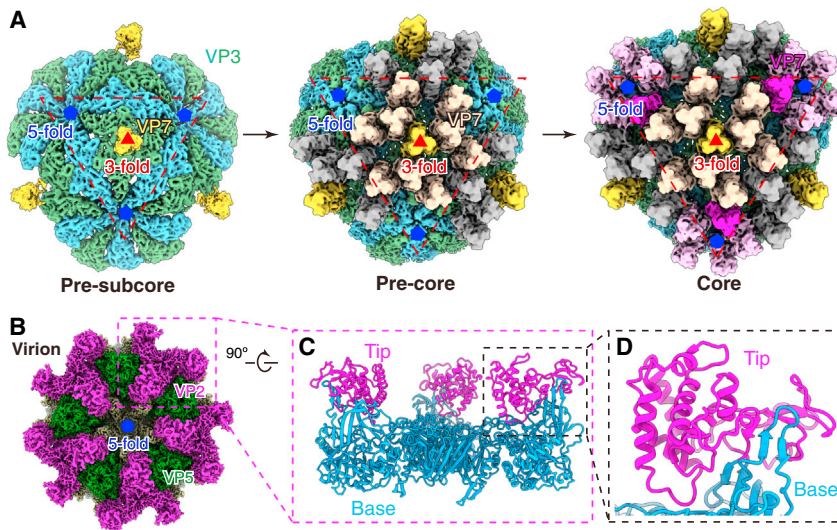


**Figure 6. Stepwise incorporation of middle-layer VP7 and outer-layer VP5 and VP2**

(A) Close-up views of the cryo-EM maps of the pre-subcore, pre-core, and core in Figure 2, highlighting the sequential addition of the VP7 trimers around the 3-fold axis. A facet of the icosahedral reconstruction in each state is indicated by a red dashed triangle. The pre-subcore is shown at a lower threshold than that in Figure 2.

(B) Cryo-EM map of the virion by sub-particle reconstruction at the 5-fold vertex.

(C and D) Structure of VP2 in ribbons showing the previously unmodeled VP2 tip domain.

### Duality model of genomic RNA packaging of BTV

Although our discovery that RNA binding promotes BTV capsid assembly is consistent with the previously proposed co-assembly model of *Reoviridae* family dsRNA

members of the *Reoviridae* family involve a single-layer, star-shaped intermediate, which expands after RNA packaging. In BTV, we observed VP6 cryo-EM density inside the capsid at 5-fold vertices (Figure 3A); by contrast, in rotavirus, a globular density was observed outside star-shaped single-layer particles and was assigned as RNA polymerase.<sup>37</sup> In the turreted reovirus, neither protein nor RNA densities were observed in the star-shaped particles at 5-fold.<sup>28</sup> Further studies would be required to test the similarity of the RNA packaging process, as homologs to BTV VP6 are yet to be discovered in rotavirus and reovirus.

### Roles of RNA in the assembly of infectious BTV capsids

The BTV genome contains 10 RNA segments, presenting a challenge for packaging all segments simultaneously into an infectious capsid. Interactions among the 10 genomic ssRNA segments and between RNA and proteins seem to offer the solution to this challenge for BTV capsid assembly.<sup>36,38,39</sup> RNA-RNA and RNA-protein interactions in rotavirus are also important for packaging all genomic RNA segments.<sup>8,40</sup> Our *in vitro* assembly assays using recombinant VP3-VP6 complex showed that binding of RNA by VP6 greatly promotes BTV capsid assembly (Figures 4B and 4C). RNA interaction with the inner surface of the VP3 shell in the BTV core has been shown to increase BTV capsid stability.<sup>41,42</sup> This VP3-RNA interaction may also function to facilitate RNA packaging and assembly of the pre-subcore. In addition, in the relatively minor species of BTV capsids that were formed without RNA (such as the empty pre-core, empty core, or empty virion in Figure S2C), no RNA polymerase VP1 was observed underneath the 5-fold vertices, indicating that RNA is also important for the incorporation of polymerase VP1 into the capsid at the 5-fold, and RNA-protein interactions possibly enhanced capsid assembly. Similarly, rotavirus RNA polymerase binds to the ends of ssRNA and is incorporated in the early assembly stage.<sup>8,43</sup> This notion of RNA-facilitation to capsid assembly is consistent with the co-assembly model of dsRNA genome packaging for infectious particles.<sup>11,12</sup>

viruses,<sup>11,12</sup> the threading of RNA through the 5-fold tunnel formed by VP3 and VP6 from outside to inside the pre-subcore resembles the core-filling model of dsRNA virus Phi6 in *Cystoviridae*.<sup>9</sup> Thus, the capture of the pre-subcore state reconciles the two sharply different and seemingly incompatible models of dsRNA virus assembly. On this basis, we propose a model of BTV assembly, which we term the *duality* model (Figures 7 and S7) because the strategy of dsRNA virus genome packaging combines elements of genome packaging strategies used by ssRNA and DNA viruses. After transcription and translation in the host cell cytoplasm, viral proteins and ssRNA segments start to assemble in the VIB. ssRNA segments interact with each other to ensure packaging of all ten segments<sup>38</sup> and promote capsid assembly through their interactions with VP6 and VP3, forming the invaginated single-layered star-subcore or pre-subcore. At this step, the adjacent vertices are assembled simultaneously by using the VP3-VP6 heterohexamers as building blocks. Parts of the RNA segments may still hang outside the capsid; the depth of VP3 invagination may depend on the amount of RNA encapsulated at this stage. In the star-subcore and pre-subcore, the VP6 pentamer binds underneath VP3 at each vertex, forming an RNA-binding tunnel through which the rest of ssRNA can thread from outside to inside the capsid. Replication of the ssRNA into dsRNA by polymerase VP1 expands the capsid, with VP6 detachment and VP1 docking at the 5-fold forming a dsRNA-filled single-layered subcore. The middle-layer protein VP7 is subsequently assembled in the VIB, forming a core, followed by addition of the outer-layer protein VP5 to form a pre-virion. Finally, a virion is formed by attachment of outer-layer protein VP2, which can interact with the cell membrane through non-structural protein NS3 to drive virus egress. Endocytosis of newly assembled virions enables a new viral replication cycle (Figure S7).

In summary, we captured eleven 3D atomic snapshots of BTV assembly. Our combination of structural analysis and functional validation has enabled a model of RNA packaging and capsid assembly for BTV. This study provides general insights into the mysteries of RNA packaging and capsid assembly of

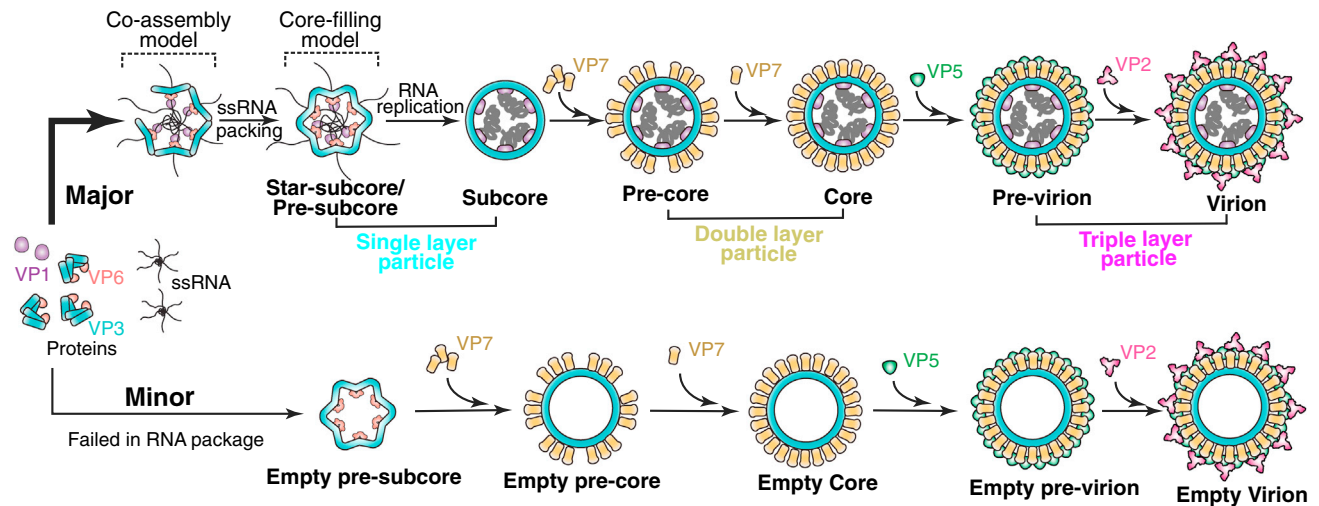


**Figure 7. The duality model of BTV RNA packaging and capsid assembly**

The assembly of BTV occurs in the host cell cytoplasm. Ten ssRNAs interact with each other to ensure packaging of all genomic RNA segments. RNA binding to the VP3-VP6 complex promotes capsid assembly into the star-subcore and pre-subcore, with RNA polymerase VP1 also incorporated (major pathway). After threading of ssRNA through the 5-fold tunnel and replication of ssRNA into dsRNA, the capsid is expanded to a spherical shape, accompanied by the replacement of VP6 by VP1 at the 5-fold axis. This duality model of BTV capsid assembly has the elements of both the co-assembly and core-filling models. The engagement of middle-layer protein VP7 starts from the capsid 3- to 5-fold axis, leading to the double-layered core. Finally, the outer-layer proteins VP5 and VP2 bind to the BTV core sequentially, resulting in the triple-layered virion. Meanwhile, the minor pathway of capsid assembly (capsid protein assembly, which failed in RNA packaging) also occurs in the host cell, leading to the empty virion.

See also [Figure S7](#).

*Reoviridae* members and beyond. Moreover, high-resolution structures of BTV assembly intermediates and the actions of VP6 rationalize the BTV vaccine based on a VP6-deficient particle.<sup>14</sup> This study advances our understanding of the RNA packaging and capsid assembly of dsRNA viruses and opens the door for designing packaging-deficient capsids as vaccines and capsid-assembly inhibitors as antivirals against these viruses.

### Limitations of the study

Although we have already described eleven states of BTV capsid assembly, we expect that other assembly intermediates, particularly transient or fast-changing ones that are thus difficult to capture, should exist in the cell. Notably, ssRNA is threaded through the 5-fold tunnel into the pre-subcore, but our study only used a short synthetic RNA. Because the number of RNA segments of members of *Reoviridae* can vary from nine to twelve and the length of these segments differs greatly within each virus, RNA packaging would be an understandably complex and dynamic process. Cryo-EM snapshots can only represent specific time points of the assembly pathway. To investigate mechanisms of RNA packaging and translocation by VP6, other methods, such as single molecular Förster resonance energy transfer (smFRET), are desirable to capture the dynamics processes of RNA packaging and capsid assembly in real time. RNA polymerase VP1 has an important role in ssRNA packaging and synthesis of the complementary RNA strand during capsid assembly, but it is not resolved in the pre-subcore of BTV, suggesting potential rearrangement, possibly with the yet-to-be-located capping enzyme.<sup>44</sup> Any roles of these “missing” en-

zymes in RNA threading through the 5-fold tunnel await future investigations.

### STAR★METHODS

Detailed methods are provided in the online version of this paper and include the following:

- [KEY RESOURCES TABLE](#)
- [RESOURCE AVAILABILITY](#)
  - Lead contact
  - Materials availability
  - Data and code availability
- [EXPERIMENTAL MODEL AND STUDY PARTICIPANT DETAILS](#)
  - Sf9 insect cells
  - BHK21 Cells
- [METHOD DETAILS](#)
  - Cell infection and vitrification
  - Focused ion beam milling
  - Acquisition and processing of cryo-ET tilt series
  - Virus isolation from infected cells
  - Cryo-EM sample preparation and image collection
  - Single-particle cryo-EM reconstruction
  - Atomic Modeling, Model Refinement and Graphics Visualization
  - Structure-guided site-directed mutagenesis and protein purification
  - Analytical Ultracentrifugation
  - *In vitro* assembly assay

- Electrophoretic mobility shift assay (EMSA)
- Reverse genetics assay
- **QUANTIFICATION AND STATISTICAL ANALYSIS**

#### SUPPLEMENTAL INFORMATION

Supplemental information can be found online at <https://doi.org/10.1016/j.cell.2024.03.007>.

#### ACKNOWLEDGMENTS

We thank Titania Nguyen for editing the manuscript. We thank Martin L. Phillips at UCLA-DOE and the biochemistry instrumentation core facility for performing the analytical ultracentrifugation. This project is supported by grants from the US NIH (AI094386 to Z.H.Z.), the Biotechnology and Biological Sciences Research Council, UK (BB/V008846/1 to P.R.), and the Wellcome Trust, UK (WT221749/20/Z, Investigator Award to P.R.). We acknowledge use of resources in the Electron Imaging Center for Nanomachines supported by UCLA; grants from the NIH (1S10OD018111) and the National Science Foundation (DBI-1338135 and DMR-1548924); and the cryo-FIB instrument in the Gonen lab supported by NIH (P41GM136508 to T.G.) and the Howard Hughes Medical Institute (to T.G.).

#### AUTHOR CONTRIBUTIONS

Z.H.Z. conceived the project and supervised research; X.X. prepared samples, recorded cryo-EM images, and processed the data; X.X. purified the protein and performed the RNA-binding assay and *in vitro* assembly assay; P.-Y.S. and P.R. performed structure-based mutagenesis and virus recovery analysis; M.W.M. in the Gonen lab generated the lamellae of infected cells grown on grids by X.X.; X.X. and Z.H.Z. interpreted results and wrote the manuscript; P.R. and P.-Y.S. edited the paper; and all authors reviewed and approved the submitted paper.

#### DECLARATION OF INTERESTS

The authors declare no competing interests.

Received: January 17, 2023

Revised: October 18, 2023

Accepted: March 7, 2024

Published: April 12, 2024

#### REFERENCES

1. Maurer, A.C., and Weitzman, M.D. (2020). Adeno-Associated Virus Genome Interactions Important for Vector Production and Transduction. *Hum. Gene Ther.* *31*, 499–511. <https://doi.org/10.1089/hum.2020.069>.
2. Liu, Y.T., Jih, J., Dai, X., Bi, G.Q., and Zhou, Z.H. (2019). Cryo-EM structures of herpes simplex virus type 1 portal vertex and packaged genome. *Nature* *570*, 257–261. <https://doi.org/10.1038/s41586-019-1248-6>.
3. Rao, V.B., and Feiss, M. (2015). Mechanisms of DNA Packaging by Large Double-Stranded DNA Viruses. *Annu. Rev. Virol.* *2*, 351–378. <https://doi.org/10.1146/annurev-virology-100114-055212>.
4. Zhou, K., Si, Z., Ge, P., Tsao, J., Luo, M., and Zhou, Z.H. (2022). Atomic model of vesicular stomatitis virus and mechanism of assembly. *Nat. Commun.* *13*, 5980. <https://doi.org/10.1038/s41467-022-33664-4>.
5. Jenni, S., Horwitz, J.A., Bloyet, L.M., Whelan, S.P.J., and Harrison, S.C. (2022). Visualizing molecular interactions that determine assembly of a bullet-shaped vesicular stomatitis virus particle. *Nat. Commun.* *13*, 4802. <https://doi.org/10.1038/s41467-022-32223-1>.
6. Chmielewski, D., Schmid, M.F., Simmons, G., Jin, J., and Chiu, W. (2022). Chikungunya virus assembly and budding visualized in situ using cryogenic electron tomography. *Nat. Microbiol.* *7*, 1270–1279. <https://doi.org/10.1038/s41564-022-01164-2>.
7. Dai, X., Li, Z., Lai, M., Shu, S., Du, Y., Zhou, Z.H., and Sun, R. (2017). In situ structures of the genome and genome-delivery apparatus in a single-stranded RNA virus. *Nature* *547*, 112–116. <https://doi.org/10.1038/nature20589>.
8. McDonald, S.M., and Patton, J.T. (2011). Assortment and packaging of the segmented rotavirus genome. *Trends Microbiol.* *19*, 136–144. <https://doi.org/10.1016/j.tim.2010.12.002>.
9. Poranen, M.M., Paatero, A.O., Tuma, R., and Bamford, D.H. (2001). Self-assembly of a viral molecular machine from purified protein and RNA constituents. *Mol. Cell* *7*, 845–854. [https://doi.org/10.1016/s1097-2765\(01\)00228-3](https://doi.org/10.1016/s1097-2765(01)00228-3).
10. Ding, K., Nguyen, L., and Zhou, Z.H. (2018). In Situ Structures of the Polymerase Complex and RNA Genome Show How Aquareovirus Transcription Machineries Respond to Uncoating. *J. Virol.* *92*. <https://doi.org/10.1128/JVI.00774-18>.
11. Roy, P. (2017). Bluetongue virus structure and assembly. *Curr. Opin. Virol.* *24*, 115–123. <https://doi.org/10.1016/j.coviro.2017.05.003>.
12. Trask, S.D., McDonald, S.M., and Patton, J.T. (2012). Structural insights into the coupling of virion assembly and rotavirus replication. *Nat. Rev. Microbiol.* *10*, 165–177. <https://doi.org/10.1038/nrmicro2673>.
13. Nooraei, S., Bahrololom, H., Hoseini, Z.S., Katalani, C., Hajizade, A., Easton, A.J., and Ahmadian, G. (2021). Virus-like particles: preparation, immunogenicity and their roles as nanovaccines and drug nanocarriers. *J. Nanobiotechnology* *19*, 59. <https://doi.org/10.1186/s12951-021-00806-7>.
14. Roy, P. (2020). Highly efficient vaccines for Bluetongue virus and a related Orbivirus based on reverse genetics. *Curr. Opin. Virol.* *44*, 35–41. <https://doi.org/10.1016/j.coviro.2020.05.003>.
15. MacLachlan, N.J., and Dubovi, E.J. (2017). Reoviridae Chapter 15. In *Fenner's Veterinary Virology, Fifth Edition* (Academic Press), pp. 299–317. <https://doi.org/10.1016/B978-0-12-800946-8.00015-5>.
16. He, Y., Shivakoti, S., Ding, K., Cui, Y., Roy, P., and Zhou, Z.H. (2019). In situ structures of RNA-dependent RNA polymerase inside bluetongue virus before and after uncoating. *Proc. Natl. Acad. Sci. USA* *116*, 16535–16540. <https://doi.org/10.1073/pnas.1905849116>.
17. Zhang, X., Patel, A., Celma, C.C., Yu, X., Roy, P., and Zhou, Z.H. (2016). Atomic model of a nonenveloped virus reveals pH sensors for a coordinated process of cell entry. *Nat. Struct. Mol. Biol.* *23*, 74–80. <https://doi.org/10.1038/nsmb.3134>.
18. Grimes, J.M., Burroughs, J.N., Gouet, P., Diprose, J.M., Malby, R., Zién-tara, S., Mertens, P.P., and Stuart, D.I. (1998). The atomic structure of the bluetongue virus core. *Nature* *395*, 470–478. <https://doi.org/10.1038/26694>.
19. Stäuber, N., Martínez-Costas, J., Sutton, G., Monastyrskaya, K., and Roy, P. (1997). Bluetongue virus VP6 protein binds ATP and exhibits an RNA-dependent ATPase function and a helicase activity that catalyze the unwinding of double-stranded RNA substrates. *J. Virol.* *71*, 7220–7226. <https://doi.org/10.1128/JVI.71.10.7220-7226.1997>.
20. Sung, P.Y., Vaughan, R., Rahman, S.K., Yi, G., Kerviel, A., Kao, C.C., and Roy, P. (2019). The Interaction of Bluetongue Virus VP6 and Genomic RNA Is Essential for Genome Packaging. *J. Virol.* *93*, e02023-18. <https://doi.org/10.1128/JVI.02023-18>.
21. Matsuo, E., Yamazaki, K., Tsuruta, H., and Roy, P. (2018). Interaction between a Unique Minor Protein and a Major Capsid Protein of Bluetongue Virus Controls Virus Infectivity. *J. Virol.* *92*, e01784-17. <https://doi.org/10.1128/JVI.01784-17>.
22. Kerviel, A., Ge, P., Lai, M., Jih, J., Boyce, M., Zhang, X., Zhou, Z.H., and Roy, P. (2019). Atomic structure of the translation regulatory protein NS1 of bluetongue virus. *Nat. Microbiol.* *4*, 837–845. <https://doi.org/10.1038/s41564-019-0369-x>.
23. Kar, A.K., Bhattacharya, B., and Roy, P. (2007). Bluetongue virus RNA binding protein NS2 is a modulator of viral replication and assembly. *BMC Mol. Biol.* *8*, 4. <https://doi.org/10.1186/1471-2199-8-4>.



24. Mohl, B.P., Kerviel, A., Labadie, T., Matsuo, E., and Roy, P. (2020). Differential Localization of Structural and Non-Structural Proteins during the Bluetongue Virus Replication Cycle. *Viruses* **12**, 343. <https://doi.org/10.3390/v12030343>.
25. Roy, P. (2020). Bluetongue virus assembly and exit pathways. *Adv. Virus Res.* **108**, 249–273. <https://doi.org/10.1016/bs.aivir.2020.08.002>.
26. Celma, C.C., and Roy, P. (2009). A viral nonstructural protein regulates bluetongue virus trafficking and release. *J. Virol.* **83**, 6806–6816. <https://doi.org/10.1128/JVI.00263-09>.
27. Kar, A.K., and Roy, P. (2003). Defining the structure-function relationships of bluetongue virus helicase protein VP6. *J. Virol.* **77**, 11347–11356. <https://doi.org/10.1128/jvi.77.21.11347-11356.2003>.
28. Sutton, G., Sun, D., Fu, X., Kotecha, A., Hecksel, C.W., Clare, D.K., Zhang, P., Stuart, D.I., and Boyce, M. (2020). Assembly intermediates of orthoreovirus captured in the cell. *Nat. Commun.* **11**, 4445. <https://doi.org/10.1038/s41467-020-18243-9>.
29. Poranen, M.M., and Bamford, D.H. (2012). Assembly of large icosahedral double-stranded RNA viruses. *Adv. Exp. Med. Biol.* **726**, 379–402. [https://doi.org/10.1007/978-1-4614-0980-9\\_17](https://doi.org/10.1007/978-1-4614-0980-9_17).
30. Nason, E.L., Rothagel, R., Mukherjee, S.K., Kar, A.K., Forzan, M., Prasad, B.V., and Roy, P. (2004). Interactions between the inner and outer capsids of bluetongue virus. *J. Virol.* **78**, 8059–8067. <https://doi.org/10.1128/JVI.78.15.8059-8067.2004>.
31. Limn, C.K., and Roy, P. (2003). Intermolecular interactions in a two-layered viral capsid that requires a complex symmetry mismatch. *J. Virol.* **77**, 11114–11124. <https://doi.org/10.1128/jvi.77.20.11114-11124.2003>.
32. Bhattacharya, B., Noad, R.J., and Roy, P. (2007). Interaction between Bluetongue virus outer capsid protein VP2 and vimentin is necessary for virus egress. *Virol. J.* **4**, 7. <https://doi.org/10.1186/1743-422X-4-7>.
33. Labadie, T., and Roy, P. (2020). A non-enveloped arbovirus released in lysosome-derived extracellular vesicles induces super-infection exclusion. *PLoS Pathog.* **16**, e1009015. <https://doi.org/10.1371/journal.ppat.1009015>.
34. Beaton, A.R., Rodriguez, J., Reddy, Y.K., and Roy, P. (2002). The membrane trafficking protein calpactin forms a complex with bluetongue virus protein NS3 and mediates virus release. *Proc. Natl. Acad. Sci. USA* **99**, 13154–13159. <https://doi.org/10.1073/pnas.192432299>.
35. Zhang, X., Boyce, M., Bhattacharya, B., Zhang, X., Schein, S., Roy, P., and Zhou, Z.H. (2010). Bluetongue virus coat protein VP2 contains sialic acid-binding domains, and VP5 resembles enveloped virus fusion proteins. *Proc. Natl. Acad. Sci. USA* **107**, 6292–6297. <https://doi.org/10.1073/pnas.0913403107>.
36. Lourenco, S., and Roy, P. (2011). In vitro reconstitution of Bluetongue virus infectious cores. *Proc. Natl. Acad. Sci. USA* **108**, 13746–13751. <https://doi.org/10.1073/pnas.1108667108>.
37. Shah, P.N.M., Gilchrist, J.B., Forsberg, B.O., Burt, A., Howe, A., Mosalaganti, S., Wan, W., Radecke, J., Chaban, Y., Sutton, G., et al. (2023). Characterization of the rotavirus assembly pathway in situ using cryoelectron tomography. *Cell Host Microbe* **31**, 604–615.e4. <https://doi.org/10.1016/j.chom.2023.03.004>.
38. Sung, P.Y., and Roy, P. (2021). RNA Origami: Packaging a Segmented Genome in Orbivirus Assembly and Replication. *Viruses* **13**, 1841. <https://doi.org/10.3390/v13091841>.
39. Sung, P.Y., and Roy, P. (2014). Sequential packaging of RNA genomic segments during the assembly of Bluetongue virus. *Nucleic Acids Res.* **42**, 13824–13838. <https://doi.org/10.1093/nar/gku1171>.
40. Fajardo, T., Sung, P.Y., Celma, C.C., and Roy, P. (2017). Rotavirus Genomic RNA Complex Forms via Specific RNA-RNA Interactions: Disruption of RNA Complex Inhibits Virus Infectivity. *Viruses* **9**, 167. <https://doi.org/10.3390/v9070167>.
41. Sung, P.Y., Zhou, Y., Kao, C.C., Aburigh, A.A., Routh, A., and Roy, P. (2023). A multidisciplinary approach to the identification of the protein-RNA connectome in double-stranded RNA virus capsids. *Nucleic Acids Res.* **51**, 5210–5227. <https://doi.org/10.1093/nar/gkad274>.
42. Gouet, P., Diprose, J.M., Grimes, J.M., Malby, R., Burroughs, J.N., Zientara, S., Stuart, D.I., and Mertens, P.P. (1999). The highly ordered double-stranded RNA genome of bluetongue virus revealed by crystallography. *Cell* **97**, 481–490. [https://doi.org/10.1016/s0092-8674\(00\)80758-8](https://doi.org/10.1016/s0092-8674(00)80758-8).
43. Lu, X., McDonald, S.M., Tortorici, M.A., Tao, Y.J., Vasquez-Del Carpio, R., Nibert, M.L., Patton, J.T., and Harrison, S.C. (2008). Mechanism for coordinated RNA packaging and genome replication by rotavirus polymerase VP1. *Structure* **16**, 1678–1688. <https://doi.org/10.1016/j.str.2008.09.006>.
44. Kumar, D., Yu, X., Crawford, S.E., Moreno, R., Jakana, J., Sankaran, B., Anish, R., Kaundal, S., Hu, L., Estes, M.K., et al. (2020). 2.7 Å cryo-EM structure of rotavirus core protein VP3, a unique capping machine with a helicase activity. *Sci. Adv.* **6**, eaay6410. <https://doi.org/10.1126/sciadv.aay6410>.
45. Mastronarde, D.N. (2005). Automated electron microscope tomography using robust prediction of specimen movements. *J. Struct. Biol.* **152**, 36–51. <https://doi.org/10.1016/j.jsb.2005.07.007>.
46. Zheng, S.Q., Palovcak, E., Armache, J.P., Verba, K.A., Cheng, Y., and Agard, D.A. (2017). MotionCorr2: anisotropic correction of beam-induced motion for improved cryo-electron microscopy. *Nat. Methods* **14**, 331–332. <https://doi.org/10.1038/nmeth.4193>.
47. Rohou, A., and Grigorieff, N. (2015). CTFIND4: fast and accurate defocus estimation from electron micrographs. *J. Struct. Biol.* **192**, 216–221. <https://doi.org/10.1016/j.jsb.2015.08.008>.
48. Bepler, T., Morin, A., Rapp, M., Brasch, J., Shapiro, L., Noble, A.J., and Berger, B. (2019). Positive-unlabeled convolutional neural networks for particle picking in cryo-electron micrographs. *Nat. Methods* **16**, 1153–1160. <https://doi.org/10.1038/s41592-019-0575-8>.
49. Zivanov, J., Otón, J., Ke, Z., von Kügelgen, A., Pyle, E., Qu, K., Morado, D., Castaño-Díez, D., Zanetti, G., Bharat, T.A.M., et al. (2022). A Bayesian approach to single-particle electron cryo-tomography in RELION-4.0. *eLife* **11**, e83724. <https://doi.org/10.7554/eLife.83724>.
50. Scheres, S.H. (2016). Processing of Structurally Heterogeneous Cryo-EM Data in RELION. *Methods Enzymol.* **579**, 125–157. <https://doi.org/10.1016/bs.mie.2016.04.012>.
51. Punjani, A., Rubinstein, J.L., Fleet, D.J., and Brubaker, M.A. (2017). cryo-SPARC: algorithms for rapid unsupervised cryo-EM structure determination. *Nat. Methods* **14**, 290–296. <https://doi.org/10.1038/nmeth.4169>.
52. Pettersen, E.F., Goddard, T.D., Huang, C.C., Meng, E.C., Couch, G.S., Croll, T.I., Morris, J.H., and Ferrin, T.E. (2021). UCSF ChimeraX: Structure visualization for researchers, educators, and developers. *Protein Sci.* **30**, 70–82. <https://doi.org/10.1002/pro.3943>.
53. Emsley, P., and Cowtan, K. (2004). Coot: model-building tools for molecular graphics. *Acta Crystallogr. D Biol. Crystallogr.* **60**, 2126–2132. <https://doi.org/10.1107/S0907444904019158>.
54. Afonine, P.V., Poon, B.K., Read, R.J., Sobolev, O.V., Terwilliger, T.C., Urzhumtsev, A., and Adams, P.D. (2018). Real-space refinement in PHENIX for cryo-EM and crystallography. *Acta Crystallogr. D Struct. Biol.* **74**, 531–544. <https://doi.org/10.1107/S2059798318006551>.
55. Kremer, J.R., Mastronarde, D.N., and McIntosh, J.R. (1996). Computer visualization of three-dimensional image data using IMOD. *J. Struct. Biol.* **116**, 71–76. <https://doi.org/10.1006/jsbi.1996.0013>.
56. Sanchez-Garcia, R., Gomez-Blanco, J., Cuervo, A., Carazo, J.M., Sorzano, C.O.S., and Vargas, J. (2021). DeepEMhancer: a deep learning solution for cryo-EM volume post-processing. *Commun. Biol.* **4**, 874. <https://doi.org/10.1038/s42003-021-02399-1>.
57. Mirdita, M., Schütze, K., Moriawaki, Y., Heo, L., Ovchinnikov, S., and Steinegger, M. (2022). ColabFold: making protein folding accessible to all. *Nat. Methods* **19**, 679–682. <https://doi.org/10.1038/s41592-022-01488-1>.
58. Jumper, J., Evans, R., Pritzel, A., Green, T., Figurnov, M., Ronneberger, O., Tunyasuvunakool, K., Bates, R., Židek, A., Potapenko, A., et al. (2021).

- Highly accurate protein structure prediction with AlphaFold. *Nature* 596, 583–589. <https://doi.org/10.1038/s41586-021-03819-2>.
59. Kucukelbir, A., Sigworth, F.J., and Tagare, H.D. (2014). Quantifying the local resolution of cryo-EM density maps. *Nat. Methods* 11, 63–65. <https://doi.org/10.1038/nmeth.2727>.
  60. Croll, T.I. (2018). ISOLDE: a physically realistic environment for model building into low-resolution electron-density maps. *Acta Crystallogr. D Struct. Biol.* 74, 519–530. <https://doi.org/10.1107/S2059798318002425>.
  61. Liu, Y.T., Zhang, H., Wang, H., Tao, C.L., Bi, G.Q., and Zhou, Z.H. (2022). Isotropic reconstruction for electron tomography with deep learning. *Nat. Commun.* 13, 6482. <https://doi.org/10.1038/s41467-022-33957-8>.
  62. Martynowycz, M.W., Zhao, W., Hattne, J., Jensen, G.J., and Gonen, T. (2019). Collection of Continuous Rotation MicroED Data from Ion Beam-Milled Crystals of Any Size. *Structure* 27, 545–548.e2. <https://doi.org/10.1016/j.str.2018.12.003>.
  63. Martynowycz, M.W., Zhao, W., Hattne, J., Jensen, G.J., and Gonen, T. (2019). Qualitative Analyses of Polishing and Precoating FIB Milled Crystals for MicroED. *Structure* 27, 1594–1600.e2. <https://doi.org/10.1016/j.str.2019.07.004>.
  64. Tacke, S., Erdmann, P., Wang, Z., Klumpe, S., Grange, M., Pitzko, J., and Raunser, S. (2021). A streamlined workflow for automated cryo focused ion beam milling. *J. Struct. Biol.* 213, 107743. <https://doi.org/10.1016/j.jsb.2021.107743>.
  65. Xia, X., and Zhou, Z.H. (2022). Using cryoEM and cryoET to visualize membrane penetration of a non-enveloped virus. *Star Protoc.* 3, 101825. <https://doi.org/10.1016/j.xpro.2022.101825>.
  66. Xia, X., Wu, W., Cui, Y., Roy, P., and Zhou, Z.H. (2021). Bluetongue virus capsid protein VP5 perforates membranes at low endosomal pH during viral entry. *Nat. Microbiol.* 6, 1424–1432. <https://doi.org/10.1038/s41564-021-00988-8>.
  67. Zivanov, J., Nakane, T., Forsberg, B.O., Kimanius, D., Hagen, W.J., Lindahl, E., and Scheres, S.H. (2018). New tools for automated high-resolution cryo-EM structure determination in RELION-3. *eLife* 7, e42166. <https://doi.org/10.7554/eLife.42166>.
  68. Ilca, S.L., Kotecha, A., Sun, X., Poranen, M.M., Stuart, D.I., and Huisken, J.T. (2015). Localized reconstruction of subunits from electron cryomicroscopy images of macromolecular complexes. *Nat. Commun.* 6, 8843. <https://doi.org/10.1038/ncomms9843>.
  69. Asanow, D., Palovcak, E., and Cheng, Y. (2019). UCSF pyem v0.5 (Zenodo) <https://doi.org/10.5281/zenodo.3576630>.
  70. Heffler, M.A., Walters, R.D., and Kugel, J.F. (2012). Using electrophoretic mobility shift assays to measure equilibrium dissociation constants: GAL4-p53 binding DNA as a model system. *Biochem. Mol. Biol. Educ.* 40, 383–387. <https://doi.org/10.1002/bmb.20649>.
  71. Boyce, M., Celma, C.C., and Roy, P. (2008). Development of reverse genetics systems for bluetongue virus: recovery of infectious virus from synthetic RNA transcripts. *J. Virol.* 82, 8339–8348. <https://doi.org/10.1128/JVI.00808-08>.

## STAR★METHODS

## KEY RESOURCES TABLE

REAGENT or RESOURCE	SOURCE	IDENTIFIER
<b>Experimental models: Organisms/strains</b>		
BTV-1 virus stain	Maintained in the lab	N/A
BHK21 cell	ATCC	CCL-10; RRID: CVCL_1914
Sf9 insect cell	Thermo Fisher Scientific	Cat# 11496015; RRID: CVCL_0549
<b>Chemicals, peptides, and recombinant proteins</b>		
Tris base	Sigma-Aldrich	Cat# 93362
Sodium chloride	Sigma-Aldrich	Cat# S6546
NP-40	Sigma-Aldrich	Cat# I8896
Triton X-100	Sigma-Aldrich	Cat# T8787
Imidazole	Sigma-Aldrich	Cat# I5513
Magnesium chloride	Sigma-Aldrich	Cat# M2670
Sucrose	Sigma-Aldrich	Cat# S7903
Glycerol	Sigma-Aldrich	Cat# G5516
N-Lauroylsarcosine sodium salt	Sigma-Aldrich	Cat# L9150
Phosphate buffer saline (PBS)	Gibco	Cat# 10010031
cOmplete Protease Inhibitor	Roche	Cat# 11836170001
DMEM	Sigma-Aldrich	Cat# D6429
Sf-9000 III SFM medium	Thermo Fisher Scientific	Cat# 12658027
Fetal Bovine Serum (FBS)	R&D Systems brand	Cat# S11150H
Penicillin/Streptomycin (100×)	HyClone	Cat# SV30010
Trypsin-EDTA (10×)	Gibco	Cat# 15400054
Uranyl acetate	Electron Microscopy Science	Cat# 22400
RNAase inhibitor RNasin	Promega	Cat# N2611
Bovine serum albumin	Sigma-Aldrich	Cat# A7030
mMACHINE T7 transcription kit	Thermo Fisher Scientific	Cat# AM1344
TBE acrylamide gels	Thermo Fisher Scientific	Cat# EC62255BOX
<b>Deposited data</b>		
Subtomogram average map of BTV virion	This study	EMD-43728
Subtomogram average map of reovirus SLP	Sutton et al. <sup>28</sup>	EMD-22165
Cryo-EM map of VP3-VP6 heterohexamer	This study	EMD-43714
Cryo-EM map of pre-subcore	This study	EMD-43719
Cryo-EM map of subcore	This study	EMD-43726
Cryo-EM map of pre-core	This study	EMD-43731
Cryo-EM map of core	This study	EMD-43730
Cryo-EM map of virion	This study	EMD-43727
Cryo-EM map of empty pre-core	This study	EMD-43725
Cryo-EM map of empty core	This study	EMD-43724
Cryo-EM map of empty virion	This study	EMD-43723
Cryo-EM map of star-subcore from <i>in vitro</i> assembly	This study	EMD-43716
Cryo-EM map of pre-subcore from <i>in vitro</i> assembly	This study	EMD-43722
Atomic model of VP2 base domain	Zhang et al. <sup>17</sup>	PDB: 3J9D
Atomic model of VP1	He et al. <sup>16</sup>	PDB: 6PNS
Atomic model of VP3-VP6 heterohexamer	This study	PDB: 8W12

(Continued on next page)



**Continued**

REAGENT or RESOURCE	SOURCE	IDENTIFIER
Atomic model of star-subcore	This study	PDB: 8W19
Atomic model of pre-subcore	This study	PDB: 8W1C
Atomic model of subcore	This study	PDB: 8W1I
Atomic model of pre-core	This study	PDB: 8W1S
Atomic model of core	This study	PDB: 8W1R
Atomic model of virion	This study	PDB: 8W1O
<b>Recombinant DNA</b>		
pFastBac1-VP3-6×His	This study	N/A
pFastBac1-VP6	This study	N/A
<b>Oligonucleotides</b>		
60 nt ssRNA oligo: gttaaaaaat cgcataaggg tccagggtac ctcttgacg tagggcgatt tcacacttac	IDT	N/A
40 nt poly-U ssRNA oligo: uuuuuuuuuu uuuuuuuuuu uuuuuuuuuu	IDT	N/A
Cy5-labeled 16 nt ssRNA oligo: cy5-gttaaaaaat cgcata	IDT	N/A
<b>Software and algorithms</b>		
SerialEM 4.0	Mastronarde <sup>45</sup>	<a href="https://bio3d.colorado.edu/SerialEM/">https://bio3d.colorado.edu/SerialEM/</a>
MotionCor2	Zheng et al. <sup>46</sup>	<a href="https://msg.ucsf.edu/software">https://msg.ucsf.edu/software</a>
CTFFIND4	Rhou and Grigorieff <sup>47</sup>	<a href="http://grigoriefflab.janelia.org/ctffind4">http://grigoriefflab.janelia.org/ctffind4</a>
Topaz v0.2.5	Bepler et al. <sup>48</sup>	<a href="https://cb.csail.mit.edu/cb/topaz/">https://cb.csail.mit.edu/cb/topaz/</a>
RELION 3.1 and 4.0	Zivanov et al. <sup>49</sup> and Scheres <sup>50</sup>	<a href="https://www3.mrc-lmb.cam.ac.uk/relion/">https://www3.mrc-lmb.cam.ac.uk/relion/</a>
cryoSPARC v4.0	Punjani et al. <sup>51</sup>	<a href="https://cryosparc.com/">https://cryosparc.com/</a>
UCSF ChimeraX 1.3	Pettersen et al. <sup>52</sup>	<a href="https://www.cgl.ucsf.edu/chimerax">https://www.cgl.ucsf.edu/chimerax</a>
Coot 0.9.6	Emsley et al. <sup>53</sup>	<a href="https://www2.mrc-lmb.cam.ac.uk/personal/pemsley/coot">https://www2.mrc-lmb.cam.ac.uk/personal/pemsley/coot</a>
Phenix 1.19.2	Afonieno et al. <sup>54</sup>	<a href="https://phenix-online.org/">https://phenix-online.org/</a>
IMOD 4.11	Kremer et al. <sup>55</sup>	<a href="https://bio3d.colorado.edu/imod/">https://bio3d.colorado.edu/imod/</a>
DeepEMhancer	Sanchez-Garcia et al. <sup>56</sup>	<a href="https://github.com/rsanchezgarc/deepEMhancer">https://github.com/rsanchezgarc/deepEMhancer</a>
AlphaFold2	Mirdita et al. <sup>57</sup> and Jumper et al. <sup>58</sup>	<a href="https://colab.research.google.com/github/sokrypton/ColabFold/blob/main/AlphaFold2.ipynb">https://colab.research.google.com/github/sokrypton/ColabFold/blob/main/AlphaFold2.ipynb</a>
ResMap 1.95	Kucukelbir et al. <sup>59</sup>	<a href="https://resmap.sourceforge.net">https://resmap.sourceforge.net</a>
ISOLDE 1.3	Croll <sup>60</sup>	<a href="https://isolde.cimr.cam.ac.uk/">https://isolde.cimr.cam.ac.uk/</a>
IsoNet v0.2	Liu et al. <sup>61</sup>	<a href="https://isonetcryoet.com/index.html">https://isonetcryoet.com/index.html</a>
<b>Others</b>		
Ultra-clear tube (SW28)	Beckman	Cat# 344058
Ultra-clear tube (SW41)	Beckman	Cat# 344059
Lacey Carbon grid with continuous ultrathin carbon	TED PELLA	Cat# 01824
Quantifoil holy grid	Electron Microscopy Science	Cat# Q2100CR1
Quantifoil holy gold grid	Electron Microscopy Science	Cat# Q2100AR2
Blotting paper, Grade 595	TED PELLA	Cat# 47000-100

**RESOURCE AVAILABILITY**

**Lead contact**

Further information and requests for resources and reagents should be directed to and will be fulfilled by the lead contact, Z. Hong Zhou ([hong.zhou@ucla.edu](mailto:hong.zhou@ucla.edu)).

### Materials availability

Materials generated by the authors in this study will be distributed upon request.

### Data and code availability

- The cryo-EM density maps were deposited in the Electron Microscopy Data Bank (EMDB) with accession code: VP3-VP6 heterohexamer (EMD-43714), pre-subcore (EMD-43719), subcore (EMD-43726), pre-core (EMD-43731), core (EMD-43730), virion (EMD-43727), empty pre-core (EMD-43725), empty core (EMD-43724), empty virion (EMD-43723), in vitro assembled pre-subcore (EMD-43722) and star-subcore (EMD-43716), and virion (EMD-43728) from subtomogram averaging. The corresponding models were deposited in the Protein Data Bank (PDB) with VP3-VP6 heterohexamer (8W12), pre-subcore (8W1C), subcore (8W1I), pre-core (8W1S), core (8W1R), virion (8W1O) and star-subcore (8W19). Subtomogram average map of reovirus SLP (EMD-22165<sup>28</sup>) was retrieved from EMDB; atomic models of VP2 (PDB:3J9D<sup>17</sup>) and VP1 (PDB:6PNS<sup>16</sup>) were retrieved from PDB.
- This paper does not report any original code.
- Any additional information required to reanalyze the data reported in this paper is available from the [lead contact](#) upon request.

## EXPERIMENTAL MODEL AND STUDY PARTICIPANT DETAILS

### Sf9 insect cells

Sf9 cells (Thermo Fisher Scientific, RRID: CVCL\_0549) were cultured in Sf-900 III SFM medium at 28°C. Cultures were maintained at  $0.5\text{--}3 \times 10^6$  cells/mL in flasks with a shaking speed of 120 rpm.

### BHK21 Cells

Baby hamster fibroblast cells BHK21 (ATCC CCL-10, RRID: CVCL\_1914) were maintained in T175 flasks at 35°C with 5% CO<sub>2</sub> in Dulbecco's modified Eagle's medium (Sigma-Aldrich) supplemented with 10% (v/v) fetal bovine serum, penicillin and streptomycin. Upon 90% cell confluence, the cells were split into fresh medium in a ratio of 1:4.

## METHOD DETAILS

### Cell infection and vitrification

Baby hamster fibroblast cells BHK21 (ATCC) were maintained at 35°C with 5% CO<sub>2</sub> in Dulbecco's modified Eagle's medium (Sigma-Aldrich) supplemented with 10% (v/v) fetal bovine serum, penicillin and streptomycin. Holy carbon-coated gold grids (Quantifoil, Q2100AR2) were sterilized with 70% ethanol and washed with fresh medium before being placed on the bottom of new flasks. The grids were then seeded with BHK21 cells at 50% confluence and incubated for 2 h before cell adhesion. Cells were infected with BTV-1 at the multiplicity of infection (MOI) of 0.5 and incubated at 35°C for about 60 h until 50% cytopathic effect (CPE) was reached (related to [Figures 1](#) and [S1A-G](#)). Grids were blotted with a Vitrobot Mark IV (Thermo Fisher Scientific) with blot force 0 for 8 s at room temperature, and plunge frozen in liquid ethane. Grids were stored in liquid nitrogen until used. For BTV assembly at early stage, cells were infected with BTV-1 at MOI of 5 and incubated for 13 h before frozen (related to [Figure S1I](#)).

### Focused ion beam milling

Grids of vitrified cells were transferred to a cryogenically cooled Aquilos (Thermo Fisher Scientific) with focused ion beam and scanning electron microscope (FIB/SEM) at liquid nitrogen temperature. To protect the cells from the damaging electron and gallium beams during the milling process, a thin layer of sputter-coated platinum was added in two steps: a fine coating, then a rough coating. After sputter coating, a thick (~300 nm) layer of carbon-rich platinum was applied to the sample using a gas injection system (GIS). The sputter-coated platinum primarily prevents charging of the sample, and the GIS platinum adds a thick coat that prevents damage to the cells during imaging or milling.<sup>62</sup> Grids were screened by collecting low magnification montages of the entire sample with the SEM. Cells infected with virus often appear as bumps in otherwise flat areas. Identified cells were targeted and individually aligned to the eucentric position. Images were taken using the FIB during each eucentric alignment to determine the shallowest possible milling angle for each position, typically 8°–22°. FIB milling was conducted as described.<sup>63</sup> Briefly, the beam of gallium ions is rastered over the sample in a rectangular area, removing unwanted material. All milling was conducted using the cleaning cross-section preset in stages. The individual milling steps consisted of trenching stress relief cuts, rough milling, medium milling, and polishing.<sup>64</sup> Rather than conducting all individual steps for each site, steps were performed for all sites sequentially, to minimize the buildup of ice contamination. All SEM images were taken at an accelerating voltage 5 kV and a beam current of 3 pA using an Everhart-Thornley detector. All FIB images were taken at an accelerating voltage of 30 kV and a beam current of 1.5 pA on the same detector. All milling was performed at an accelerating voltage of 30 kV. Beam currents were as follows: 1 nA for milling stress relief cuts and rough milling, 300 pA for medium milling, and 30 pA for polishing. Grids containing milled lamellae were transferred to liquid nitrogen Dewars prior to tilt series collection by Titan Krios electron microscope.

### Acquisition and processing of cryo-ET tilt series

The good lamellae were loaded into a 300 kV Titan Krios electron microscope (Thermo Fisher Scientific) equipped with a Gatan imaging filter (GIF) Quantum LS and a Gatan K3 Summit direct electron detector. Tilt series were collected at a nominal magnification of 33,000 $\times$ , corresponding to a calibrated pixel size of 2.6 Å at specimen level. Tilt series between  $-60^\circ$  and  $+40^\circ$  with a tilt increment of  $3^\circ$  were acquired using a grouped dose-symmetric tilt scheme start at  $-10^\circ$  (or between  $-40^\circ$  and  $+60^\circ$  with a start at  $10^\circ$ , according to the pre-tilt angle of the lamella) in serialEM.<sup>45</sup> Defocus was set between  $-3.5\ \mu\text{m}$  and  $-4.5\ \mu\text{m}$ . A movie of 6 frames was recorded at each tilt angle, and the total cumulative dosage for each tilt series was about 100 electrons/Å<sup>2</sup>.

Frames in each movie were motion corrected by MotionCor2<sup>46</sup> without dose weighting. Defocus value of the aligned image in each tilt angle was estimated by CTFFIND4.<sup>47</sup> Tilt series were reconstructed by patch tracking, and tomograms were generated by weighted back projection with SIRT-like filter and binned 4 $\times$  (10.4 Å per pixel) with IMOD 4.11 software package.<sup>55</sup> Deep learning-based software package IsoNet<sup>61</sup> was used for missing wedge compensation and denoising. Tomograms were rendered in ChimeraX<sup>52</sup> by using the volume tracer.

Different assembly intermediates of BTV were picked separately in IMOD, and their coordinates were imported into RELION 4.0<sup>49</sup> for subtomogram averaging (see Table S1). First, the picked particles were extracted as pseudo-tomograms with box size of 200 in bin2 (5.2 Å per pixel) and refined with icosahedral symmetry. Sub-particles at each vertex (12 vertices from 1 capsid) were then extracted in bin1 (2.6 Å per pixel) with box size of 200 by using the angular and shift parameters from icosahedral refinement. These particles were reconstructed with C5 symmetry and subjected to local refinement. Tomo CTF refinement and Tomo frame alignment were subsequently performed and followed by particle re-extraction and 3D refinement. After the first cycle of refinement (Tomo CTF refinement, Tomo frame alignment, particle re-extraction and 3D refinement), the particles were subjected to 3D classification without alignment. The cycle of refinement was repeated three times until converging. This procedure of subtomogram averaging was performed for BTV virion and empty virion, with a final sub-particle reconstruction at 7.2 Å and 9.0 Å, respectively. For BTV pre-subcore, core, pre-virion, and empty core/empty pre-virion (empty core and empty pre-virion were not able to be separated in the current workflow due to limited particle number), particles were extracted with box size of 300 pixels and reconstructed with icosahedral symmetry to resolutions of 28 Å, 25 Å, 32 Å and 32 Å, respectively. For these intermediates, no improvements were obtained by sub-particle reconstruction. See summary of data collection and subtomogram averaging in Figure S1 and Table S1.

### Virus isolation from infected cells

The isolation procedure of BTV viral particles was the same as described before.<sup>65,66</sup> Briefly, ten flasks of BHK21 (ATCC) cells at 90% confluence were infected with BTV-1 at MOI of 0.1 and harvested at 90% CPE about 70 h post infection. Infected cells were collected with a cell scraper and lysed with 20 mL lysis buffer (100 mM Tris-HCl, pH 8.8, 50 mM NaCl, 0.1% v/v NP40 and protease inhibitor) at 4°C for 15 min. Cell debris was removed by centrifugation at 2,000 g for 10 min. 10 mL 50% (w/v) sucrose buffer (20 mM Tris-HCl, pH 8.8, 50 mM NaCl, 0.2% v/v NP40, 50% w/v sucrose) was layered on top 4 mL of 66% (w/w) sucrose buffer (20 mM Tris-HCl, pH 8.8, 50 mM NaCl, 0.2% v/v NP40, 66% w/w sucrose) in an ultra-clear tube (Beckman). The sample was loaded onto the double cushion and centrifuged with a SW28 rotor at 100,000 g for 1 h at 4°C. The virus band at the interface of the two sucrose cushions was collected and diluted 10 times in 20 mM Tris-HCl at pH 8.8. N-Lauroylsarcosine sodium salt (Sigma-Aldrich) at final concentration of 0.1% was added to the sample and incubated on ice for 10 min. The sample was cleared by centrifugation at 16,000 g for 10 min, and the supernatant was pelleted through 1 mL 30% (w/v) sucrose cushion in SW 41 Ti rotor at 80,000 g for 1 hour at 4°C. Finally, the pellet with virus was resuspended in 20  $\mu\text{L}$  of 20 mM Tris-HCl at pH 8.8.

### Cryo-EM sample preparation and image collection

For the BTV capsid isolated from infected cells, cryo-EM grids were prepared with thin continuous carbon film-coated lacey grids (Ted Pella) by using Vitrobot Marker IV. 2.5  $\mu\text{L}$  of viral isolate was applied to a glow-discharged grid. After incubation for 1 min, the grid was blotted for 20 s at 8°C with 15 blot force and 100% humidity and plunge-frozen in liquid ethane. For recombinant VP3-VP6 complex, 3  $\mu\text{L}$  protein at concentration of 1 mg/mL was loaded to a glow-discharged holy carbon grid (Quantifoil 2/1, Electron Microscopy Science) and blotted for 9 s with blot force of 4 in Vitrobot. For the *in vitro* assembled capsid, purified VP3-VP6 complex at a final concentration of 1 mg/mL was mixed with a 40 nt poly-U ssRNA oligo (final concentration of 100  $\mu\text{M}$ ) in binding buffer (10 mM Tris 7.5, 50 mM NaCl, 5 mM MgCl<sub>2</sub>, 1 mM DTT). After 20 min incubation at room temperature, 3  $\mu\text{L}$  of the sample was loaded to a glow-discharged holy carbon grid (Quantifoil 2/1) and blotted for 9 s with blot force of 4 in Vitrobot. The grid was then plunge-frozen in liquid ethane and stored in liquid nitrogen.

The grids with proper ice thickness and particle concentrations were loaded to a Titan Krios electron microscope (Thermo Fisher Scientific) operated at 300 kV in super-resolution mode. The microscope was equipped with a Gatan K3 direct electron detector and a Gatan energy filter (slit width of 20 eV). A nominal magnification of 81,000 $\times$  was used, corresponding to a calibrated pixel size of 0.55 Å on the specimen level in super-resolution mode. Defocus was set from  $-1.8$  to  $-2.6\ \mu\text{m}$ . Movies were recorded with exposure time of 2 s, dose-fractionated into 40 frames, in SerialEM,<sup>45</sup> leading to a total dosage of  $\sim 50$  electrons/Å<sup>2</sup> on the specimen. A total of 62,928 movies were collected by using beam image-shift in a ten-day session for the capsids isolated from infected cells; 2,843 movies were collected for the recombinant VP3-VP6 complex; 9,015 movies were collected for the *in vitro* assembled capsids.



### Single-particle cryo-EM reconstruction

The workflow of single-particle analysis of the viral isolate is summarized in [Figure S2](#) and [Table S2](#). Each movie was motion-corrected by MotionCor2<sup>46</sup> and binned 2× to a pixel size of 1.1 Å. The defocus values of micrographs were determined by CTFFIND4.<sup>47</sup> A total of 2,154,042 virus particles were picked by Topaz,<sup>48</sup> a convolutional neural networks-based particle picking software. The particles were extracted in RELION 3.1<sup>50,67</sup> and binned 2× to a pixel size of 2.2 Å with a box size of 400×400 pixels to accelerate computation. 330,212 good particles were selected from the first round of 2D classification and subsequently subjected to a second round of 2D classification. Particles of single layer (29,474 particles), double layer (76,750 particles) and triple layer (180,815 particles) are clearly different in the averaged images of 2D classification; they were selected from the second round of 2D classification and subjected to further 2D and 3D analysis in RELION separately. A total of eight different BTV assembly states were obtained by 3D classification with icosahedral symmetry: 25,227 particles in pre-subcore, 177 particles in subcore, 46,654 particles in pre-core, 10,865 particles in empty pre-core, 16,121 particles in core, 2,335 particles in empty core, 140,565 particles in virion, and 40,250 particles in empty virion. To analyze the RNA density inside the pre-subcore, 3D classification with a spherical mask at the inner capsid space was performed on the 25,227 pre-subcore particles (insertion in [Figure S2](#)). A final set of 2,424 particles were obtained with better RNA density, shown in [Figure 3A](#).

To improve the resolution, the eight assembly states were separately subjected to icosahedral-structure-guided sub-particle reconstruction.<sup>2,68</sup> The *STAR* files of viral particles from icosahedral reconstruction were symmetry expanded by using the *relion\_particle\_symmetry\_expand* command in RELION. Duplicated particle entries with the same coordinates were removed, resulting in twelve sub-particles of the 5-fold vertices (C5 symmetry) from one virus particle. For the pre-subcore and subcore, a box size of 320×320 pixels (bin1, 1.1 Å/pixel) was used; for the other six assembly states, a box size of 384×384 pixels (bin1, 1.1 Å/pixel) was used.

For the pre-subcore, 302,724 sub-particles were extracted. An initial map was generated by using the *relion\_reconstruct* command, with shift and rotation parameters obtained from icosahedral refinement. After auto-refinement, the sub-particles were subjected to 3D classification in RELION without alignment. Two conformations (67,371 particles in Conf1 and 96,003 particles in Conf2) differing at the 5-fold invagination of VP3 were selected. Maps of Conf1 and Conf2 with C5 symmetry were obtained after 3D auto-refinement and CtfRefinement in RELION at a resolution of 3.6 Å and 3.7 Å, respectively. The map of Conf1 was used for further analysis in this paper due to better density of VP6.

For the virion, 1,686,780 sub-particles were extracted. After 3D auto-refinement with C5 symmetry, the density of VP1 (RNA dependent RNA polymerase) at 5-fold axis was smeared due to symmetry mismatch. To resolve the structure of VP1, these sub-particles were expanded 5 times by C5 symmetry and subjected to local classification (K=7) without alignment with a spherical mask at 5-fold axis. Five of the seven classes contain good densities of VP1; each one has a different VP1 orientation. One class of 1,483,715 particles (17.5%) was selected and subjected to further 3D classification, auto-refinement and CtfRefinement. A final map of 2.8 Å with C1 symmetry was obtained from 498,646 particles.

For the subcore, 2,124 sub-particles were extracted and subjected to 3D auto-refinement and CtfRefinement. A map of 6.5 Å with C5 symmetry was obtained. Due to the limited particle number, local classification with a mask at 5-fold axis failed to resolve the asymmetric density of VP1. For pre-core and core, the same strategy as that for the virion was applied. Final maps of 3.1 Å and 3.3 Å with C1 symmetry were obtained for pre-core and core, respectively. For the empty pre-core, empty core and empty virion, no VP1 density at 5-fold axis was observed. The final maps with C5 symmetry were obtained after 3D classification, auto-refinement and CtfRefinement at 3.2 Å, 3.5 Å and 2.9 Å for empty pre-core, empty core and empty virion, respectively.

The reconstruction workflow of recombinant VP3-VP6 complex is summarized in [Figure S3](#). 1,451,665 particles (box size 256×256 pixels, 1.1 Å/pixel) were autopicked from 2,843 motion-corrected micrographs in cryoSPARC<sup>51</sup> and 683,281 particles were selected based on the good features in 2D class averages. The initial model was generated from these particles with ab initio reconstruction in cryoSPARC. Particle coordinates were imported into RELION for further classification and refinement by using the *csparc2star.py*<sup>69</sup> script. After 3D classification and refinement, 626,185 particles were subjected to 3D classification without alignment; classes with variations at VP3 apical domain were separated. A class with 138,115 particles was selected and subjected to CtfRefinement. A final map of 3.5 Å was obtained, containing 4 VP3 molecules and 2 VP6 molecules (VP3-VP6 heterohexamer). In the same dataset, some assembled single layer capsids were observed and manually picked from the micrographs. 718 picked particles were reconstructed in icosahedral symmetry. After symmetry expansion, twelve vertices were extracted from each virus particle. 8,395 sub-particles with box size of 320×320 pixels (bin1, 1.1 Å/pixel) were obtained. Finally, a map of VP3-VP6 capsid vertex at 4.7 Å was obtained after 3D classification without alignment, 3D refinement and CtfRefinement in RELION.

The reconstruction workflow of the *in vitro* assembled capsid is summarized in [Figure S5](#). Each movie was motion corrected by MotionCor2<sup>46</sup> and binned 2× to a pixel size of 1.1 Å. The defocus values of micrographs were determined by CTFFIND4.<sup>47</sup> A total of 3,614 micrographs with good particles were selected from 9,015 collected images after a manual screen. 7,478 particles were manually picked and subjected to 2D and 3D classification in RELION.<sup>50,67</sup> Two conformations of the assembled particles with different VP3 invagination were obtained: 1,411 particles in star-subcore and 5,336 particles in pre-subcore. After symmetry expansion, twelve vertices were extracted from each virus particle. 16,932 sub-particles and 64,032 particles with box size of 320×320 pixels (bin1, 1.1 Å/pixel) were obtained for star-subcore and pre-subcore, respectively. For star-subcore, 7,837 particles were selected after 3D classification without alignment in RELION, resulting in a final map of 4.4 Å with C5 symmetry after CtfRefinement. Similar to that

of pre-subcore in the viral isolate of infected cells, two conformations were obtained from the pre-subcore of the *in vitro* assembly capsids. 17,277 particles in Conf1 were selected for further analysis, resulting in a map of 3.5 Å with C5 symmetry.

The cryo-EM maps were auto-sharpened by the DeepEMhancer.<sup>56</sup> Both the unsharpened and sharpened maps were uploaded into the Electron Microscopy Data Bank (EMDB). The local resolution evaluations were determined by ResMap.<sup>59</sup>

### Atomic Modeling, Model Refinement and Graphics Visualization

All the atomic models were initially built in Coot<sup>53</sup> according to the cryo-EM maps from DeepEMhancer sharpening. For pre-subcore, VP3A and VP3B were built ab initio; the pentameric density that binds to VP3 at the 5-fold axis was assigned as VP6 according to the side chain densities. VP6 CBD (a.a. 1-33 and 262-329) was built in Coot according to the density, while RBD (130-261) was built with guidance of model from AlphaFold2.<sup>57,58</sup> The model was then refined in ISOLDE<sup>60</sup> and Phenix<sup>54</sup> and validated by the wwPDB validation server. For the modeling of VP3-VP6 heterohexamer and star-subcore, models of VP3A, VP3B, VP6 CBD and RBD from pre-subcore were docked into the cryo-EM map as rigid bodies in UCSF ChimeraX<sup>52</sup> and manually adjusted in Coot. Models of BTV virion (VP3 and VP1: PDB:6PNS; VP2: PDB:3J9D) from previous studies<sup>16,17</sup> were fitted into our cryo-EM map of the virion. The tip domain of VP2 (a.a. 190-408) was newly built according to its density. The model was then manually adjusted in Coot and refined in ISOLDE and Phenix. The refined model of BTV virion was used for model building of subcore, pre-core and core. All models were refined in ISOLDE<sup>60</sup> and Phenix<sup>54</sup> and validated by the wwPDB validation server. Visualization of the atomic model, including figures and movies, was accomplished in UCSF ChimeraX.<sup>52</sup>

### Structure-guided site-directed mutagenesis and protein purification

VP3-VP6 complex used for cryo-EM, *in vitro* assembly assay and EMSA was overexpressed by the Bac-to-Bac baculovirus expression system in insect cell sf9. The DNA sequence encoding VP3 was cloned into a pFastBac1 vector with an N-terminal hexahistidine tag. VP6 was cloned into a pFastBac1 vector without tag. Mutants were generated by QuikChange mutagenesis and confirmed by DNA sequencing. Baculoviruses for VP3 and VP6 were generated separately. Sf9 cells at density of  $2.5 \times 10^6$ /mL were coinfecting with baculoviruses of VP3 and VP6 at a ratio of 3:1. Cells were incubated at 28°C, 120 rpm for three days before harvest at a cell viability of 80%. After centrifugation at 2,000 g for 10 min, the cells were resuspended and lysed on ice for 15 min in a buffer containing 100 mM Tris 7.5, 100 mM NaCl, 1% Triton X-100 and protease inhibitors comprising 1 mM PMSF, 1 mM benzamidine, 2.5 µg/mL aprotinin, 5 µg/mL leupeptin. After high-speed centrifugation at 30,000 g for 30 min, the supernatant was loaded to a column with HisPur cobalt resin (Thermo Fisher Scientific). The beads were then washed with 50 column volume of wash buffer containing 20 mM Tris 7.5, 500 mM NaCl and 20 mM imidazole and eluted with elution buffer containing 20 mM Tris 7.5, 100 mM NaCl and 250 mM imidazole. Proteins were further purified by ion-exchange column (Source-15Q, GE Healthcare) and followed by gel-filtration column (Superose 6, GE Healthcare) in buffer containing 10 mM Tris 7.5, 100 mM NaCl, 1 mM DTT. The purified proteins were concentrated and stored at -80°C.

### Analytical Ultracentrifugation

Analytical ultracentrifugation experiments were performed in a Beckman Optima XL-A analytical ultracentrifuge (Beckman Coulter). Sedimentation equilibrium experiments were carried out at purified protein concentrations of 0.15, 0.45 and 0.6 mg/mL in 20 mM Tris-HCl, pH 7.5, 150 mM NaCl. The experiments were performed at 20°C and at two different speeds of 6,000 and 10,000 rpm, and data were collected at 280 nm. Weight average molecular masses were determined by fitting the data of 6,000 rpm with a nonlinear least-squares exponential fit for a single ideal species using Beckman Origin-based software. The baseline was floated to partially correct for some contaminating lower molecular weight proteins which at this low speed do not redistribute significantly.

### *In vitro* assembly assay

The 60 nt ssRNA oligo was synthesized in Integrated DNA Technologies (IDT). Sequence of the oligo (5'-gttaaaaaatcgcataagggtc cagggtactcttgacgtgagggcgatttcacacttac-3') was designed by combining the 5' and 3' sequence of BTV segment 9. Genomic RNA segment 10 was generated by T7 transcription from cDNA as before.<sup>39</sup> Purified VP3-VP6 complex at final concentration of 0.1 mg/mL was mixed with the 60 nt ssRNA oligo (final concentration of 40 µM) in binding buffer composed of 10 mM Tris 7.5, 50 mM NaCl, 5 mM MgCl<sub>2</sub>, 1 mM DTT and 2 U/µL RNAase inhibitor RNasin (Promega). For capsid assembly on genomic RNA segment 10 (shown in Figure S4E), a final concentration of 2 µM RNA was used. The protein-RNA mixture was incubated at room temperature for 20 min and then subjected to negative stain analysis with an FEI 200 kV T20 microscope equipped with a Gatan Ultra-scan US4000 4k camera (Figures 4C and S4C). Images were taken at a nominal magnification of 50,000×. For each sample, a set of 20 images was collected at random positions. The total number of assembled particles was counted from the 20 images. Alternatively, the assembly reactions of 100 µL were pelleted through 100 µL 30% sucrose cushion in a TLA100.1 rotor at 100,000 g for 30 min (Figure 4B). The pellets were analyzed by SDS-PAGE and quantified by using ImageJ software. The assembly assays were repeated three times at the biological level.

### Electrophoretic mobility shift assay (EMSA)

The RNA binding activity of the VP3-VP6 complex was assessed through EMSA. 5 nM Cy5-labeled 16 nt ssRNA (cy5'-gttaaaaaatcgcata) was mixed with increasing amounts of protein in 10-µL reactions in 10 mM Tris-HCl, pH 7.5, 50 mM NaCl, 5 mM MgCl<sub>2</sub>, 10%

glycerol, 0.1 mg/mL bovine serum albumin and 2 U/ $\mu$ L RNAase inhibitor RNAsin (Promega) in DEPC-water. After incubation on ice for 30 min, the samples were resolved by electrophoresis on 4-20% gradient native TBE acrylamide gels (Invitrogen) in 0.5 $\times$  TBE on ice. The fluorescent bands were detected with a Bio-Rad ChemiDoc XRS+ system and quantified using ImageJ software. The bound fractions were quantified according to the disappearance of free RNA relative to the intensity of the control lane. The data were fitted to a simple binding equation:  $F = A \times P_0 / (K_d + P_0)$ , where F is the fraction of RNA bound, A is the maximal fraction of RNA bound,  $P_0$  is the concentration of total protein, and  $K_d$  is the equilibrium binding constant.<sup>70</sup> The apparent binding affinity ( $K_{1/2}$ ) values were estimated from the protein concentration at 50% saturation. The experiments were repeated three times at the biological level.

### Reverse genetics assay

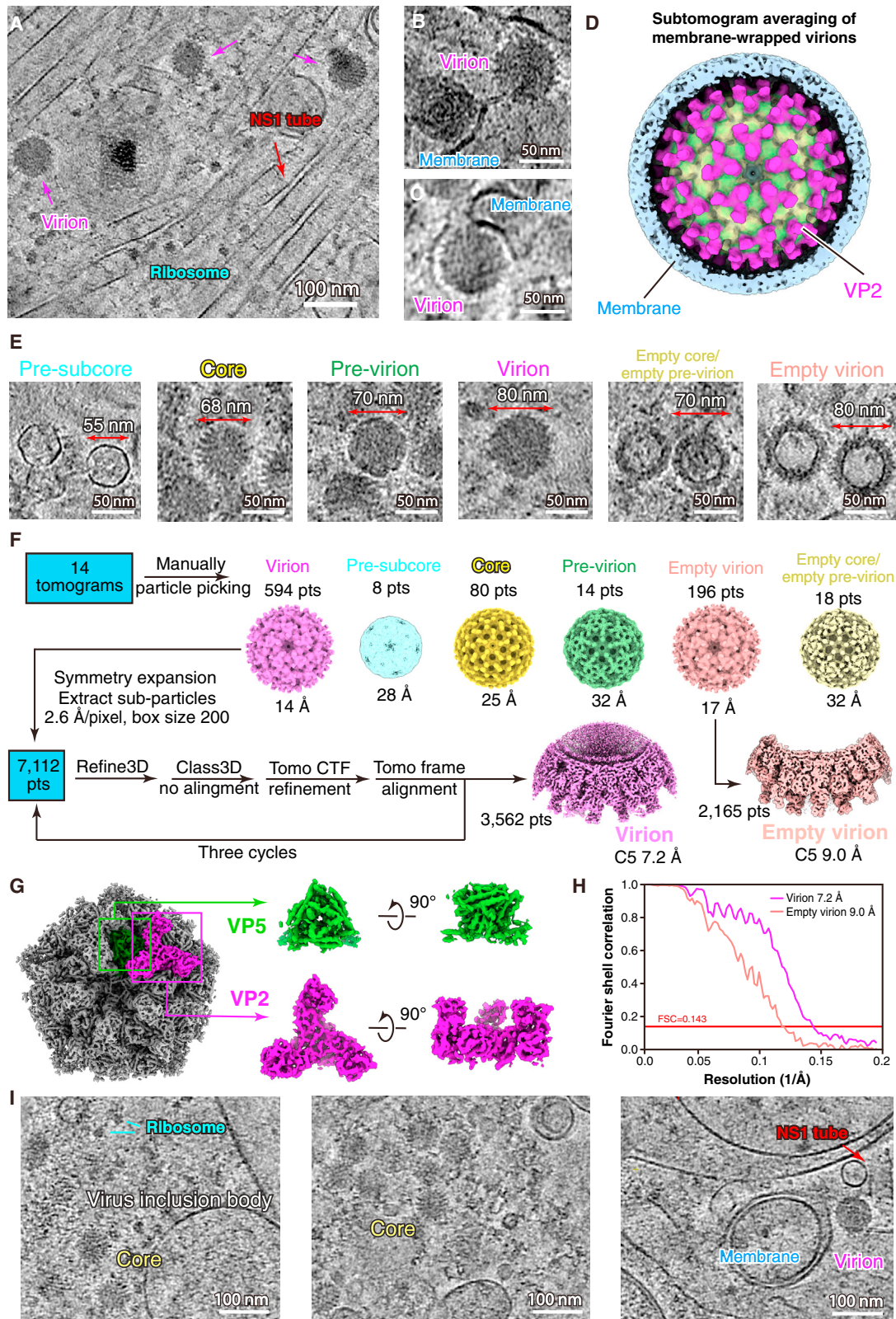
Site-directed mutagenesis was performed to introduce mutations into the exact copy of BTV-1 S3 or S9 (pUC19 BTV1-T7S3 or pUC19 BTV1-T7S9) cDNA plasmid for reverse genetics assay, as previously described.<sup>71</sup> Briefly, BTV RNA transcripts were generated by digesting the cDNA plasmids using a mMACHINE T7 transcription kit (Thermo Fisher Scientific). A monolayer of BSR cell (derived from BHK21 cell) in six-well plates at 100% confluence was transfected with a mixture of ten different BTV RNA transcripts (either WT or mutant) using Lipofectamine 2000 reagent. The medium was removed at 4 hours post transfection, and 6 mL new medium consisting of 2% FBS and 1.5% (w/v) agarose was layered on top the cell. The plates were incubated at 35°C in 5% CO<sub>2</sub> for 72 hours for plaque formation.

### QUANTIFICATION AND STATISTICAL ANALYSIS

Data were presented as means (s.d.) calculated from three biological replicates. Data were analyzed with ImageJ and Origin Pro software. [Figure 3I](#) were fitted by a simple binding equation to calculate the apparent binding affinity ( $K_{1/2}$ ). All the details can be found in the figure legends and [method details](#).



# Supplemental figures



(legend on next page)

---

**Figure S1. BTV assembly intermediates and membrane interactions captured by cryo-ET, related to Figure 1**

(A) A slice image from a cryo-ET reconstruction, showing BTV virions in host cell cytoplasm. Cells were infected with BTV at a multiplicity of infection (MOI) of 0.5 and frozen at 60 h after infection.

(B and C) Slice images from Figure 1G showing virion-membrane interactions.

(D) Subtomogram averaging of the membrane-wrapped virions from Figure 1G showing VP2 in the vicinity of the membrane.

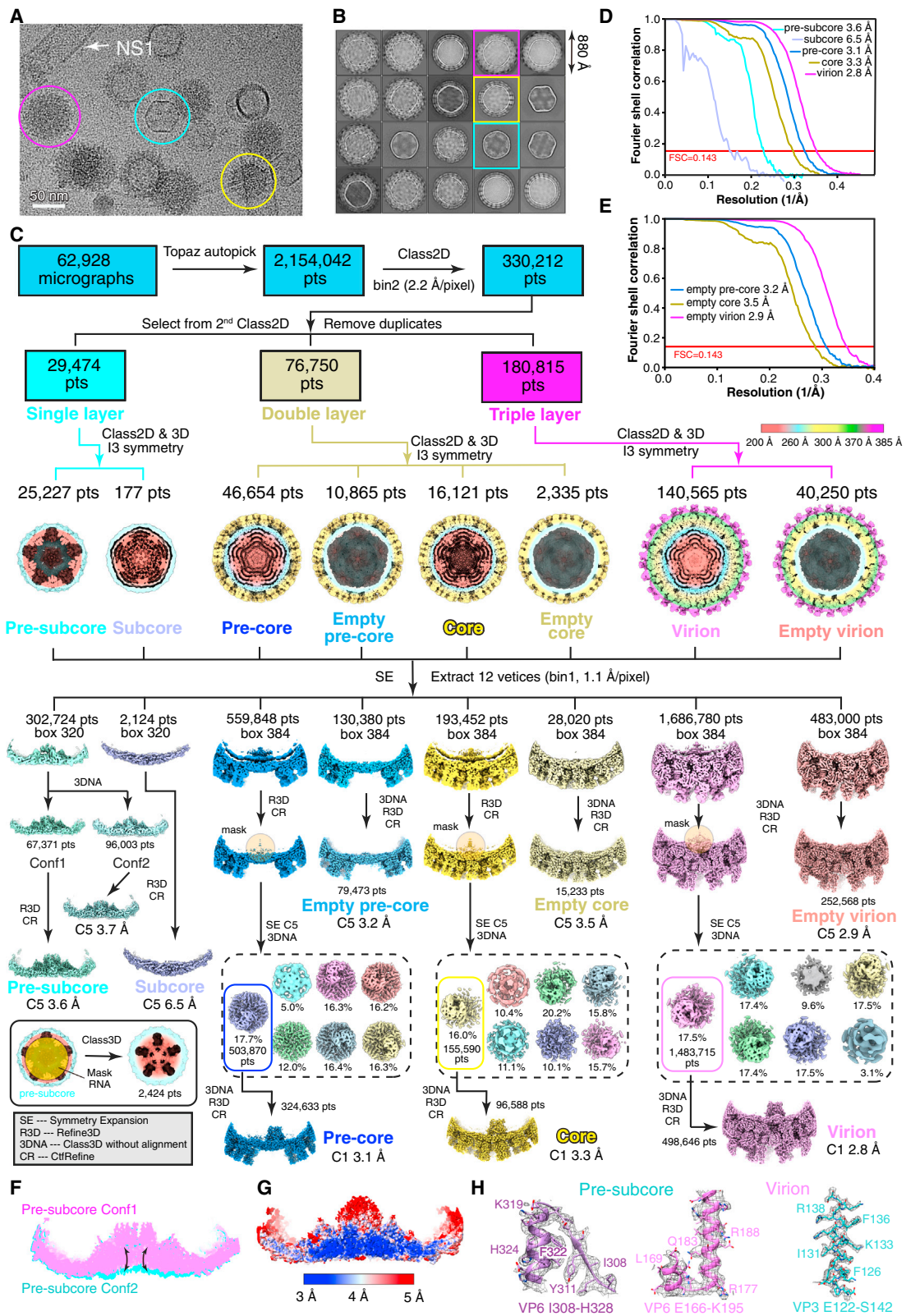
(E) BTV assembly states captured by cryo-ET, including pre-subcore, core, pre-virion, and virion, as well as empty core/empty pre-virion and empty virion.

(F) Workflow of subtomogram averaging.

(G) Density map of virion after subtomogram averaging, showing the well-resolved  $\alpha$  helices.

(H) Gold-standard Fourier shell correlation (FSC) curves for subtomogram averaging of virion and empty virion.

(I) Slices from cryo-ET reconstructions showing BTV assembly in host cell cytoplasm. Cells were infected with BTV at a MOI of 5 and frozen at 13 h after infection.



(legend on next page)

---

**Figure S2. Cryo-EM data processing of the BTV capsids isolated from infected cells, related to Figure 2**

(A) Representative cryo-EM image of isolated capsids from infected cells. Cyan, yellow, and magenta circles indicate the single-, double-, and triple-layered particle, respectively.

(B) Selected 2D class averages of the cryo-EM particles.

(C) Flow chart of cryo-EM data processing showing the eight assembly states.

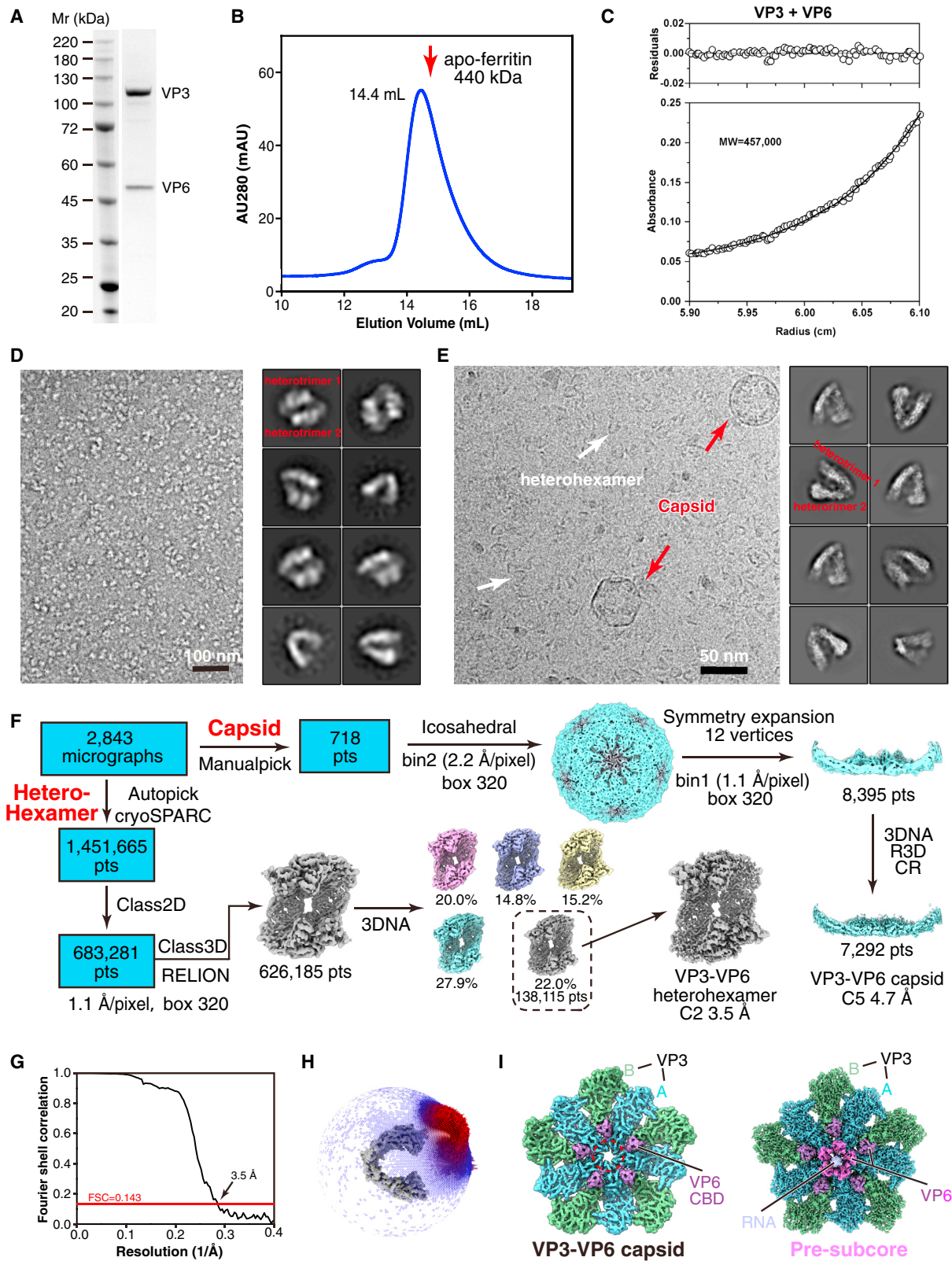
(D and E) Gold-standard Fourier shell correlation (FSC) curves for 3D reconstructions.

(F) Superposition of the maps of pre-subcore Conf1 and Conf2.

(G) Local resolution of sub-particle map of pre-subcore Conf1.

(H) Representative cryo-EM density maps of pre-subcore and virion.





(legend on next page)

---

**Figure S3. Characterization of recombinant VP3-VP6 complex, related to Figures 3 and 4**

(A and B) SDS-gel (A) and gel-filtration chromatography (B) of the recombinant VP3-VP6 complex. Arrow indicates the elution volumes of apo-ferritin (~440 kD) as a marker. Results represent three independent purification experiments.

(C) Representative results from equilibrium sedimentation of analytical ultracentrifugation. Data were collected at 20°C, at a rotor speed of 6,000 rpm, with absorbance measured at 280 nm. The molecular weight of the VP3-VP6 complex was measured to be 457 kDa.

(D) Negative stain TEM analysis of the recombinant VP3-VP6 complex. Images of 2D class averages are shown on the right of the panel.

(E) Cryo-EM analysis of the recombinant VP3-VP6 complex. Images of 2D class averages are shown on the right of the panel.

(F) Flow chart of cryo-EM data processing of the recombinant VP3-VP6 complex.

(G and H) Gold-standard Fourier shell correlation (FSC) curves (G) and angular distribution of particles used in final refinement (H) for 3D reconstructions of VP3-VP6 heterohexamer.

(I) Comparison of 5-fold tunnel of capsids assembled in the absence and presence of ssRNA.

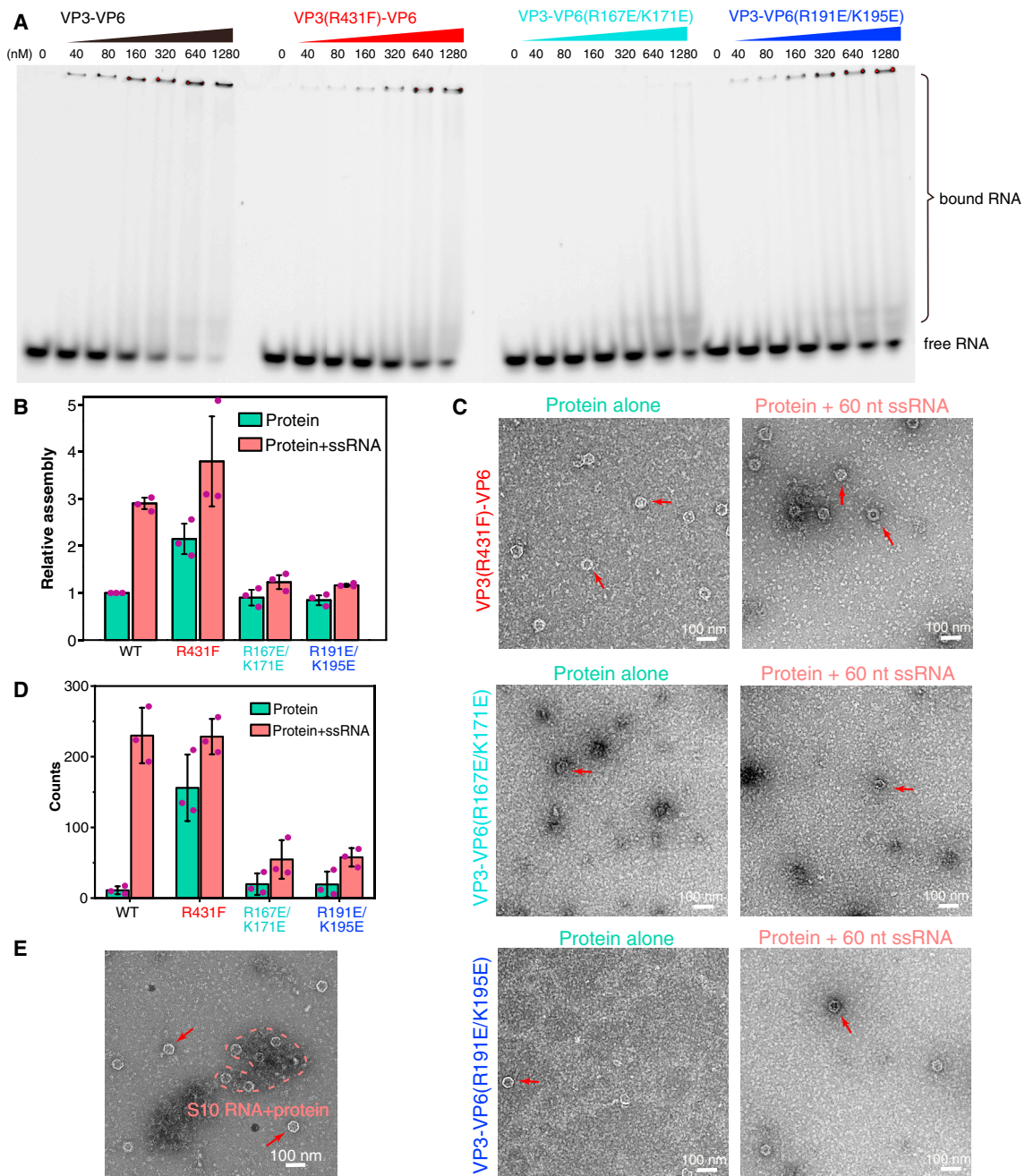


**Figure S4. RNA binding and capsid assembly of recombinant proteins, related to Figures 3 and 4**

(A) EMSA of the RNA-binding activities of the VP3-VP6 complex with the WT interface or RNA-binding mutants. 5 nM Cy5-labeled 16 nt ssRNA was mixed with increasing amounts of protein. The samples were resolved by electrophoresis on 4%–20% gradient native TBE acrylamide gels. Representative images from three biological repeats are shown here. The bound fractions were quantified as the disappearance of free RNA and shown in Figure 3I.

(B) Quantification of the assembled capsids from the *in vitro* assembly assay represented by SDS-PAGE in Figure 4B. Error bars, SD ( $n = 3$  independent measurements).

(C) Negative staining TEM images of recombinant VP3-VP6 complexes with RNA-binding mutations in the absence and presence of 60 nt ssRNA. Red arrows point to the assembled capsids.

(D) Quantification of the assembled capsids from *in vitro* assembly assay represented by negative staining from Figures 4C and S4C. Error bars, SD ( $n = 3$  independent measurements).

(E) Negative staining TEM images of the recombinant VP3-VP6 complex incubated with S10 ssRNA of the BTBV genome. Red arrows point to assembled capsids. Dashed circle indicates a large protein-RNA aggregate.

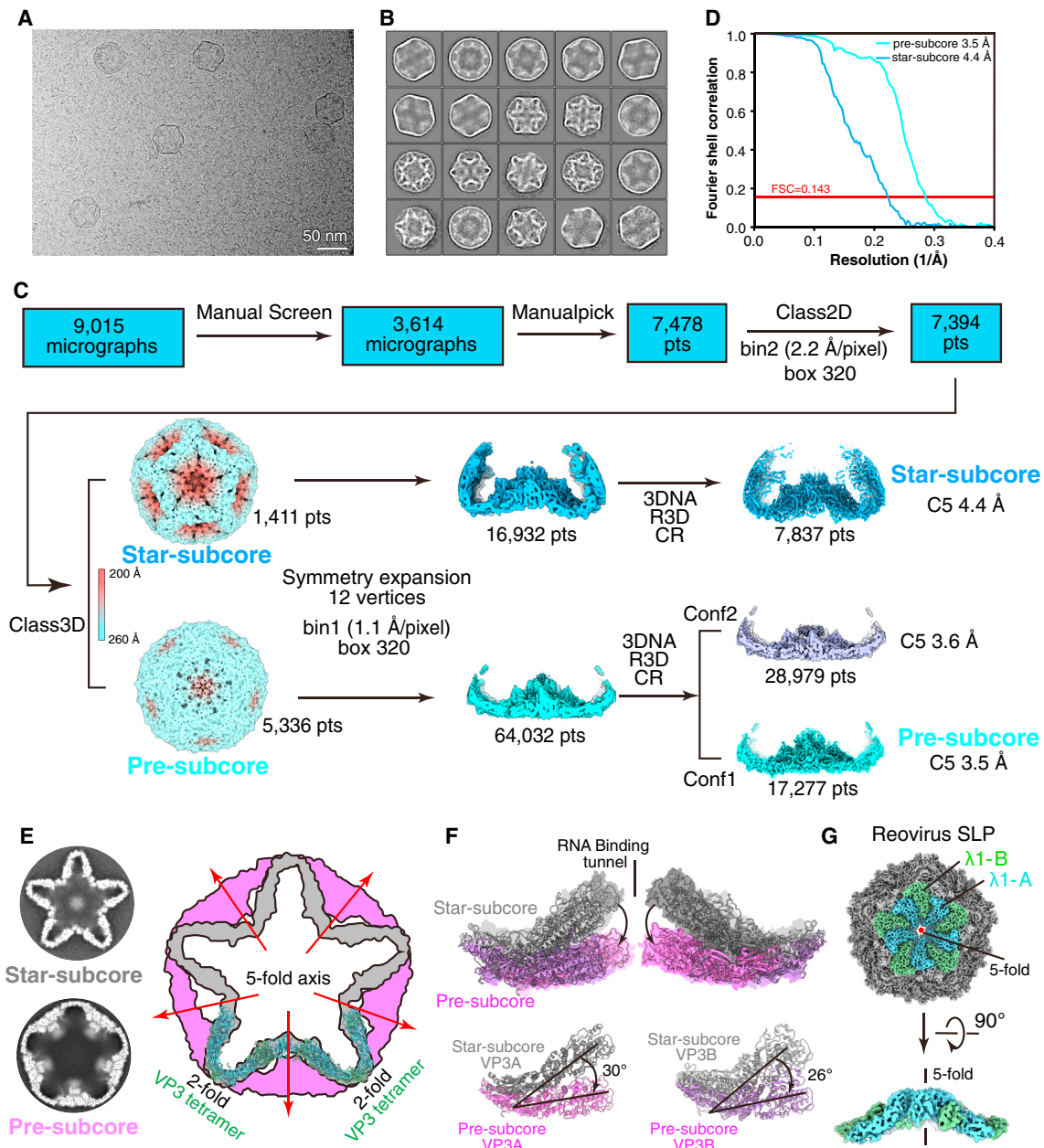


**Figure S5. Structure of the *in vitro*-assembled BTV capsid from recombinant proteins, related to Figure 4**

(A) Representative cryo-EM image of the *in vitro*-assembled capsid.

(B) Selected 2D class averages of the cryo-EM particles.

(C) Flow chart of cryo-EM data processing. Two configurations (star-subcore and pre-subcore) of the assembled capsid are sorted by classification. The structure of pre-subcore from *in vitro*-assembled capsids is identical to that of pre-subcore from viral isolate. Within the two conformations (Conf1 and Conf2) in the pre-subcore, Conf1, which has better resolution and map density, is used for further analysis.

(D) Gold-standard Fourier shell correlation (FSC) curves for 3D reconstructions.

(E) Comparison of star-subcore and pre-subcore. Structure of VP3-VP6 heterohexamers is aligned with star-subcore at the icosahedral 2-fold axis.

(F) Structure superposition of star-subcore and pre-subcore showing the conformational change of VP3 at 5-fold axis.

(G) Cryo-EM map of the single-layered particle of reovirus capture by cellular tomography.<sup>28</sup>



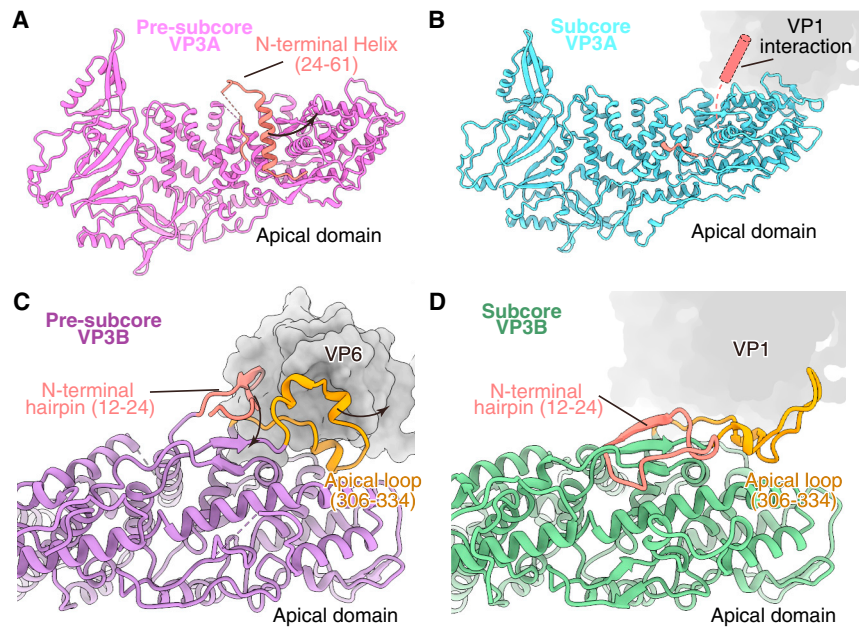


**Figure S6. Local conformational changes of VP3 during RNA packaging, related to Figure 5**

(A and B) Structures of VP3A in the pre-subcore (A) and subcore (B) showing the separation of the N-terminal helix (aa 24–61). This helix sits atop the VP3 apical domain in the pre-subcore (A); it is invisible (represented as a cylinder) in the subcore (B) and is able to bind to VP1. Black arrows in (A) indicate the movements of the N-terminal helix.

(C and D) Structures of VP3B in the pre-subcore (C) and subcore (D) showing conformational changes of the N-terminal  $\beta$ -hairpin (aa 12–24) and apical loop (aa 306–334). N-terminal  $\beta$ -hairpin and apical loop dock to the surface of VP6 in the pre-subcore (C) and are restructured for VP1 binding in the subcore (D). Black arrows in (C) indicate the movements of the N-terminal  $\beta$ -hairpin and apical loop.

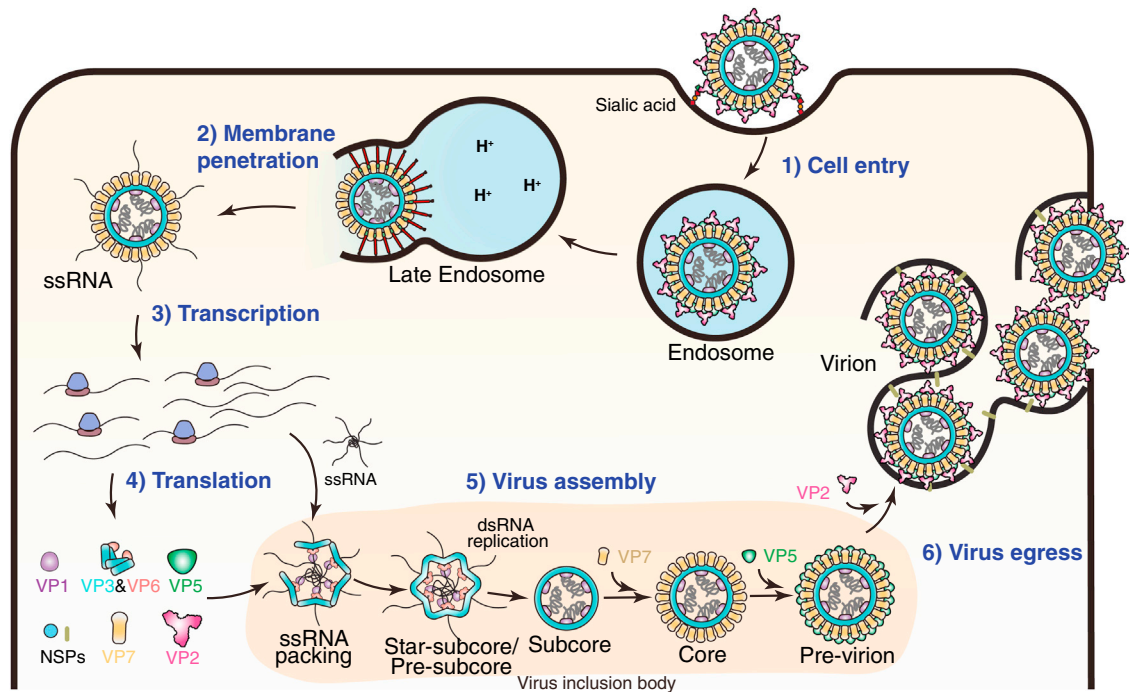


**Figure S7. Mechanistic model of BTV replication cycle, related to Figure 7**

Virus enters host cells via sialic acid binding by VP2, followed by endocytosis.<sup>35</sup> Low pH in the late endosome triggers detachment of VP2 and conformational changes of VP5. The long stalk of VP5 can penetrate the endosomal membrane and release BTV core into the host cell cytosol,<sup>66</sup> where transcription of the core is activated. After transcription and translation, viral proteins and ssRNA segments start to assemble in the virus inclusion body. Ten ssRNA segments interact with each other and promote capsid assembly by interactions with VP6 and VP3, forming the invaginated single-layered pre-subcore. In the pre-subcore, the VP6 pentamer binds underneath VP3 at each vertex, forming an RNA-binding tunnel through which the ssRNA can thread from outside to inside of the capsid. Replication of the ssRNA into dsRNA by polymerase VP1 expands the capsid, forming the dsRNA-filled, single-layered particle subcore. The middle-layer protein VP7 and out-layer protein VP5 are then subsequently assembled in the virus inclusion body, leading to core and pre-virion, respectively. Virion is formed by engagement of the out-layer protein VP2, which can interact with the cell membrane through NS3 to enable virus egress<sup>26</sup> and start of a new replication cycle.